united nations
educational, scientific
and cultural
organization

international atomic
energy agency

the
abdus salam
international centre for theoretical physics

H4. SMR/1247
Lecture Note: 01

WORKSHOP ON PHYSICS OF MESOSPHERE-STRATOSPHERE-TROPOSPHERE INTERACTIONS WITH SPECIAL EMPHASIS ON MST RADAR TECHNIQUES

(13 - 24 November 2000)

MST RADAR INTERFEROMETRY

Prof. Jurgen ROTTGER

Max-Planck-Institut fur Aeronomie
Katlenburg-Lindau
GERMANY

School on Atmospheric Radar
- SAR -

Tirupati/Gadanki, India, 10-13 Dec. 1997

Lecture L-5
Preliminary Lecture Notes

MST Radar Interferometry

Jürgen Röttger

MST radars have conventionally been used in the Doppler-Beam-Swinging and the Spaced-Antenna modes to study the dynamics and the structure of the lower and middle atmosphere.

During the past decade also the radar interferometry and radar imaging, which base on the spaced antenna system configuration, have been introduced in MST radars and have been applied very successfully. This allows many new features of the scattering and reflecting structures to be investigated as well as yields improved information, such as: measurements of incidence/tilt angles, deduction and improvement of velocity estimates, gravity wave parameters, tracking of scattering patches, imaging of spatial structure and information on the inhomogeneity in the scattering volume etc.

We will summarize in this lecture the basics of radar interferometry in a tutorial way without going into the complex theory and mathematics rather than trying to explain the basics in a most elementary and perceptive way, to make the method and its advantages best understandable and attractive for newcomers in this field. The theory, methodical details, derivations and other sophisticated application methods are found in publications compiled in the included list of references.

The contents of this lecture, and in particular of these lecture notes, are mostly a collection of excerpts from published papers as well as several presentations of the author, blended with some new provisions. In such preliminary notes there are admittedly resulting some inconsistencies in the nomenclature and some unavoidable duplications or meek imperfections, which should be removed in a final version of these preliminary lecture notes.

November 15, 1997

D 00/a

L-5 **MST Radar Interferometry** School on Atmospheric Radar

NMRF, Tirupati/Gadanki, India, 10-13 Dec. 1997

Jürgen Röttger

Dr. Jürgen Röttger, EISCAT Scientific Association, S-981 28 Kiruna, Sweden
from 1 Jan. 1998: Max-Planck-Institut für Aeronomie, D-37191 Katlenburg-Lindau, Germany

Introduction

Radar Interferometry

Interferometry using radio waves had been widely employed and developed in radio astronomy, lightning detecting and positioning, and originally as early as in radio frequency direction finding. We may call these passive interferometer methods, since the detected and analyzed signals were not originated from or generated by the observer himself.

Radar interferometry detects and analyses echoes, which result from targets illuminated by an active transmitter, which is (usually) controlled by the observer. This means that sensible signals can be analyzed only if they are radio detected and ranged (radar). Interferometry had been applied in addition to the standard radar methods, in particular for remote sensing of the topography of the Earth, moon and planets. The former is done by synthetic aperture radars (SAR), the latter is known as planetary radar.

The first application of radar interferometry was done for ionospheric incoherent scatter radar studies by Woodman (1971). Farley et al. (1981) did first radar interferometry studies of ionospheric irregularities.

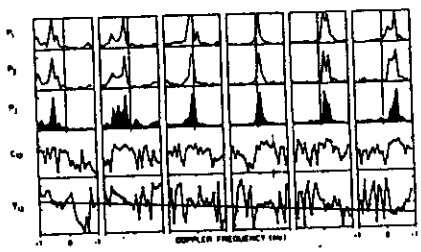

The first MST radar studies (see figure) were published by Röttger and Ierkic (1985), while initial experiments, showing the applicability of basic interferometry with MST radars, were performed as early as 1978 by Röttger and Vincent. Here we will present a basic tutorial of MST radar interferometry, together with examples of a variety of observations with this and related methods with MST radar.

Any contemporary phased-array MST radar system should nowadays be equipped with interferometer capabilities, as we will demonstrate in this lecture.

Interferometry is applying measurements of the phases of radio waves to increase the spatial resolution of radar targets, i.e. the atmospheric/ionospheric structure in the case of MST-radar imaging.

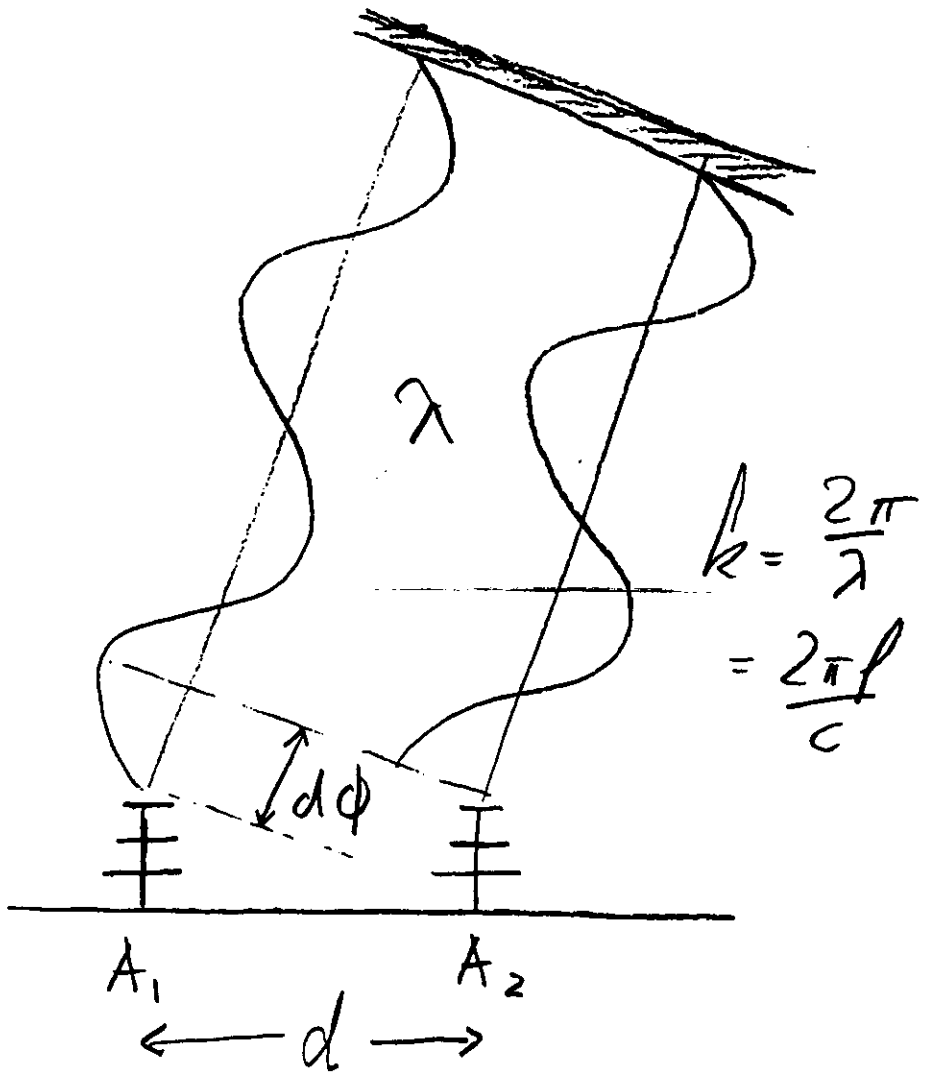

The **spatial domain interferometry (SDI)** applies the measurement of phases of radar echoes on one wavelength (frequency) at two or more antennas displaced in horizontal space. This improves the resolution in the horizontal plane.

An equivalent to the spatial domain interferometry is the frequency domain interferometry, where the spatial co-ordinates d in the SDI are replaced by wavelengths λ (i.e. different frequencies $f = c/\lambda$).

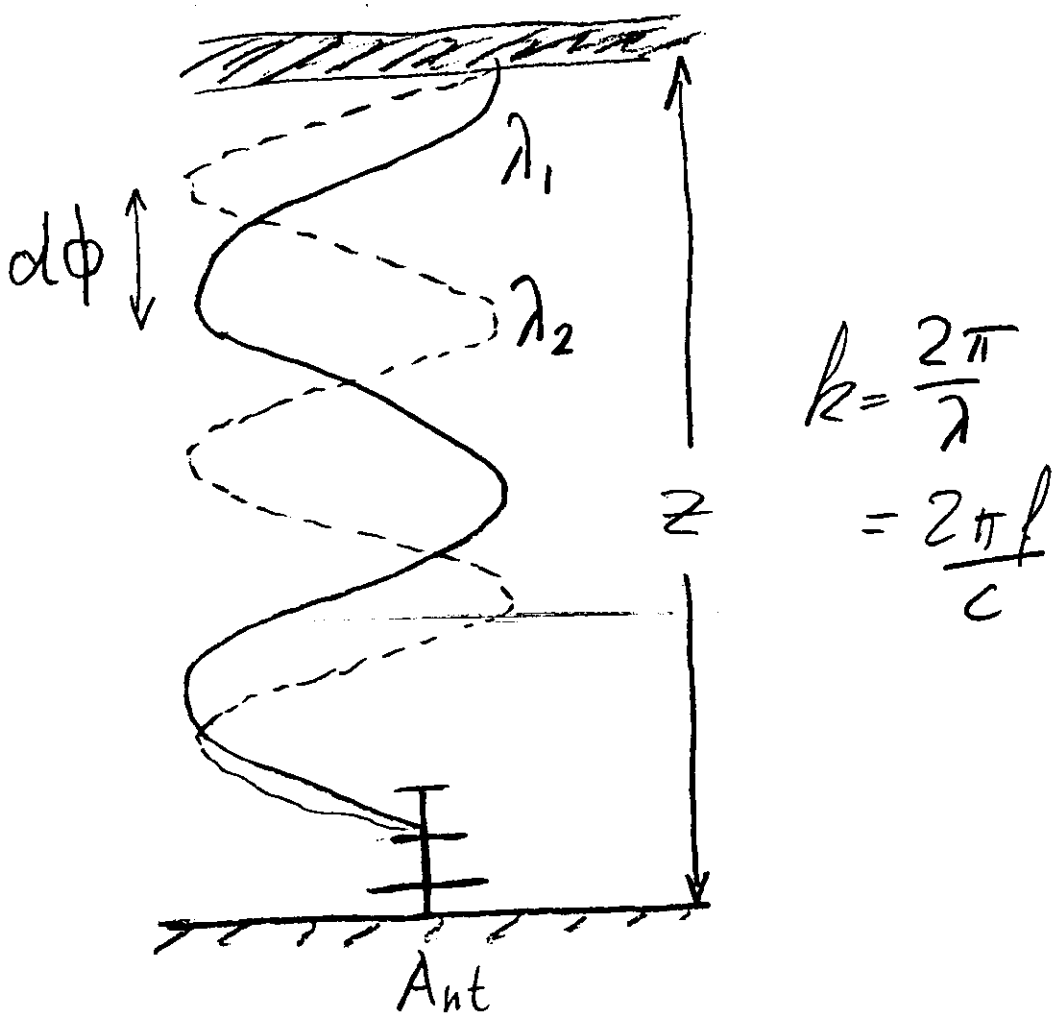

The **frequency domain interferometry (FDI)** applies the measurement of phases of radar echoes on two or more wavelengths (frequencies) at one antenna. This improves the resolution in the vertical direction.

D03

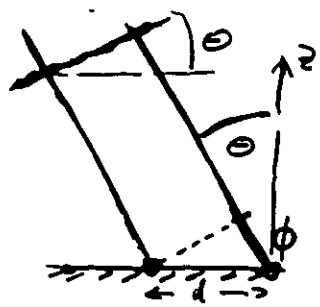

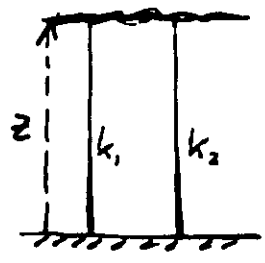

$\Delta\phi = k\, d \sin\Theta$

$\Delta\phi = z\,(k_2 - k_1)\cdot z$

① $\Delta\phi \rightarrow \Theta$
→ tilt angle position

② coherence
$\Gamma(\omega)$ → horiz. persistance

③ horiz displacement
↳ ≈ velocity

1) $\Delta\phi \rightarrow z$

2) coherence →
vert. layer persistence
≙ layer thickness

3) vertical displacement

Phase differences measured with SDI at two antennas are directly related to the zenith or tilt angle Θ. The spectrum analysis also yields information about the horizontal persistence (correlation distance) and horizontal displacements of scattering/reflecting structures, i.e. the horizontal velocity.

Phase differences measured with FDI on two frequencies yield the exact range of a scattering/reflecting structure and the vertical displacement as well as the vertical structure persistence, i.e. the structure thickness.

DO4.

Just as a short excursion we like to present some data resulting from frequency domain interferometry (FDI) of thin layers in the mesosphere. It is possible to determine the layer thickness and the layer position, i.e. its relative change as function of time. The data analysis method is described by Franke et al., and will not be repeated here. In the following we will just concentrate on the spatial domain interferometry (SDI).

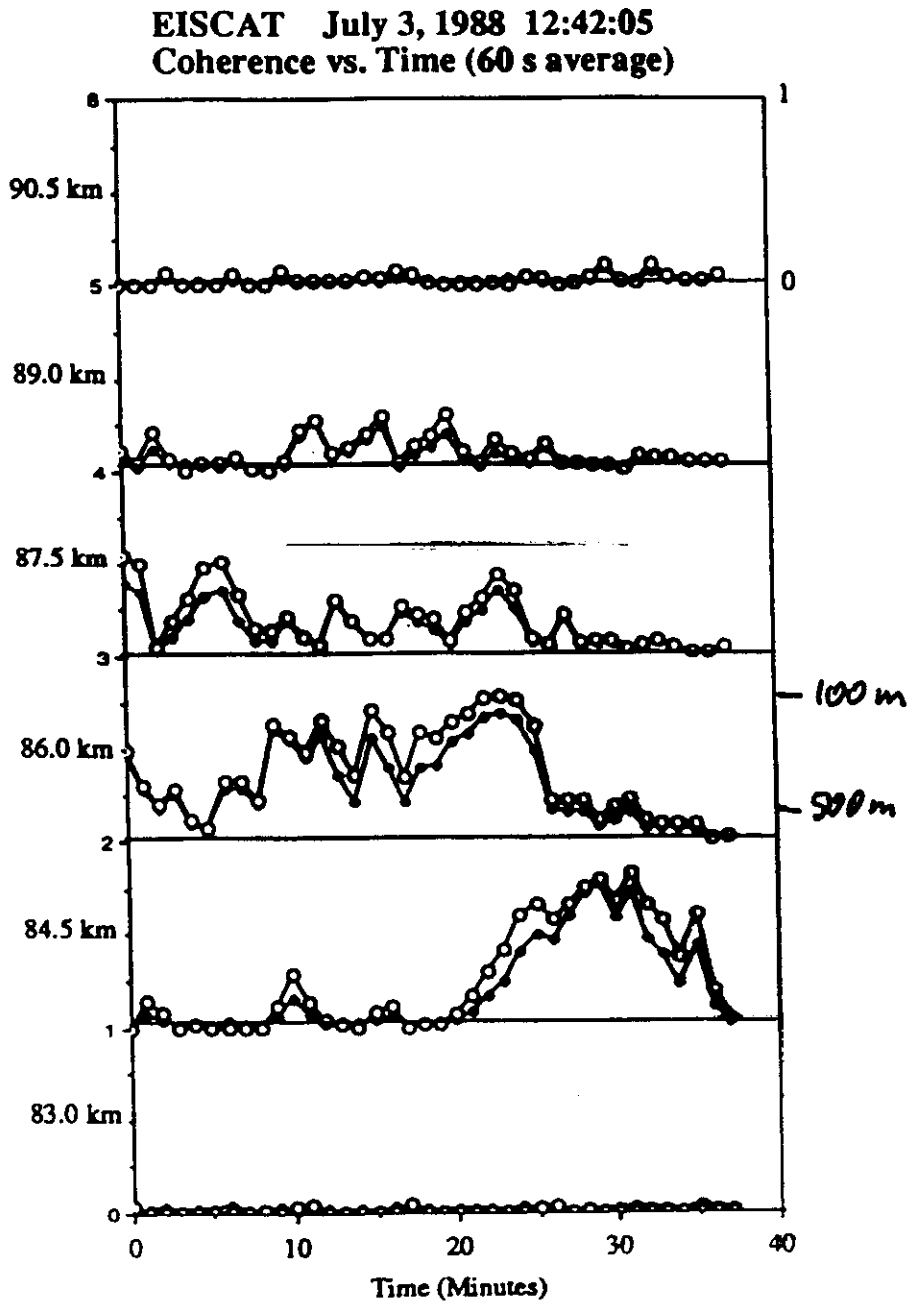

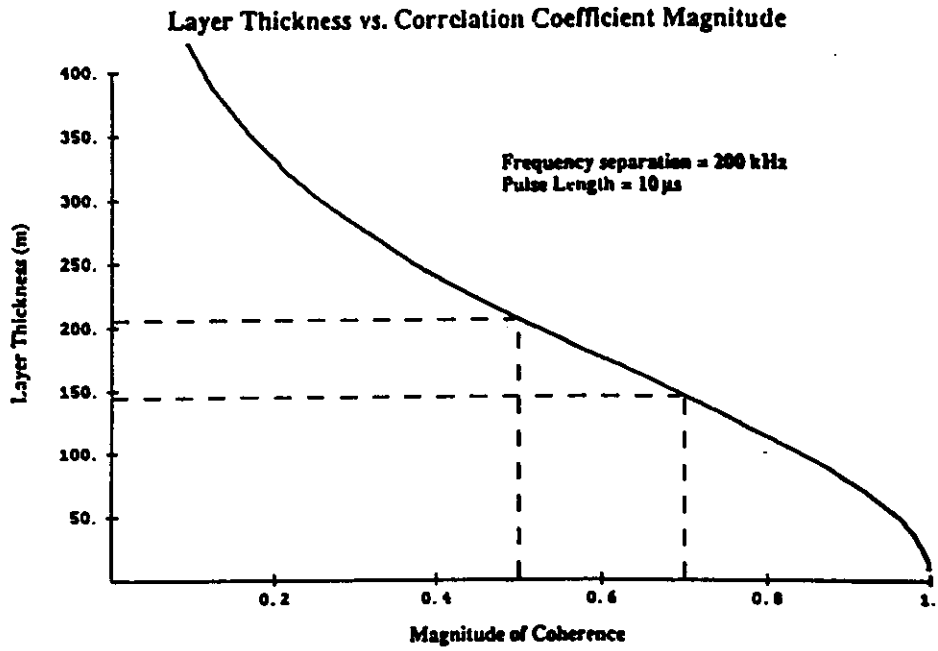

Fig. 1. Theoretical relationship between the magnitude of the coherence coefficient and the thickness of the scattering layer for the 200-kHz frequency separation and 10-μs pulse length used in the experiment.

FDI

FRANKE ET AL.: FREQUENCY DOMAIN INTERFEROMETRY WITH EISCAT VHF RADAR

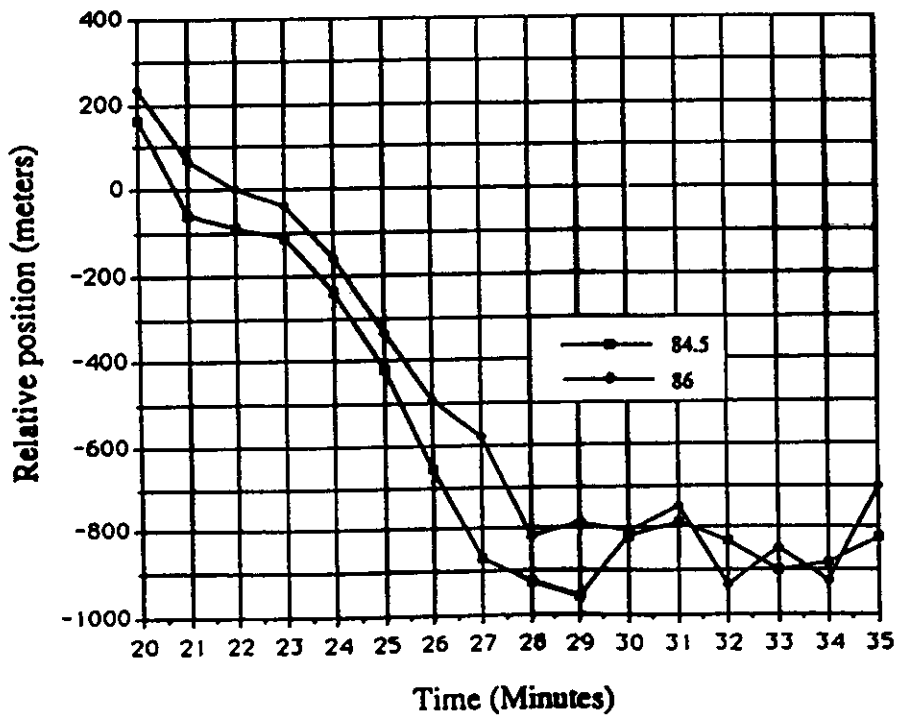

Fig. 6. The relative position of the thin scattering layer as estimated from the phase of the coherence coefficient for the interval when the spectrogram indicates downward and accelerating motion.

C06

To apply radar interferometry, some basics of **phased array antenna systems** are repeated here. Essentially, the directional characteristics of the antenna systems, i.e. the antenna pattern, are a basic requisite of this technique.

The main parameter determining the antenna gain and the corresponding beam width is the size or the area of the antenna, which is also called the antenna aperture. The antenna aperture can be either regarded as a continuous radiator if it is illuminated by an independent feed system, or it can consist of several sub-elements which are electrically fed from a common transmitter source. Both approaches can be basically treated by a similar formalism, which we will explain for the simple case of a line of antenna dipole elements. Assume that N individual antenna elements with equal spacing d are horizontally lined up to form a multi-element array (see Fig. 10). In the array far-field ($r > (Nd)^2/\Lambda_o$) the antenna polar diagram is

$$E(\delta) = \sum_{n=1}^{N} E_n(\delta)\exp\left(i\left(\frac{2\pi(n-1)d}{\Lambda_o}\sin\delta + \Phi_n\right)\right),$$

where $E_n(\delta)$ is the pattern of an individual element and Φ_n is a relative phase placed on this element. Thus, the polar diagram is just the Fourier transform of the spatial aperture distribution. If all the elements have similar $E_n(\delta)$ and Φ_n, the polar diagram is a function sin Nx/sin x with $x = \pi \cdot d \cdot \sin\delta/\Lambda_o$. If $d < \Lambda_o$, there is only one main lobe at $\delta = 0°$ (for $\varphi = 0$). If $d > \Lambda_o$, grating lobes at $\delta_G = \arcsin(\Lambda_o/d)$ occur, for $E_n(\delta) =$ const with amplitudes similar to the main lobe. The width of the main lobe is $\delta_B = \arcsin(\Lambda_o/Nd)$. In radar applications also the two-way beam width ~~$\delta_B/\sqrt{2}$ is used.~~ If δ_B is small, it is directly proportional to the ratio of the wavelength Λ_o to the aperture dimension Nd. The radiation pattern has minima (nulls in theory) at $\delta_n = \pm n\delta_B$, where n = 1,2,..., N/2, and sidelobes occur at $\delta_s = \delta_n \pm \delta_B/2$. If equal weighting W_n is applied to each of the single elements (e.g., $E_n'(\delta) = W_n \cdot E_n(\delta)$, with W_n = const for all n), the first sidelobe closest to the main lobe is suppressed by 13.2 dB plus the fall-off of the individual element pattern $E_n(\delta)$ at δ_{s1}.

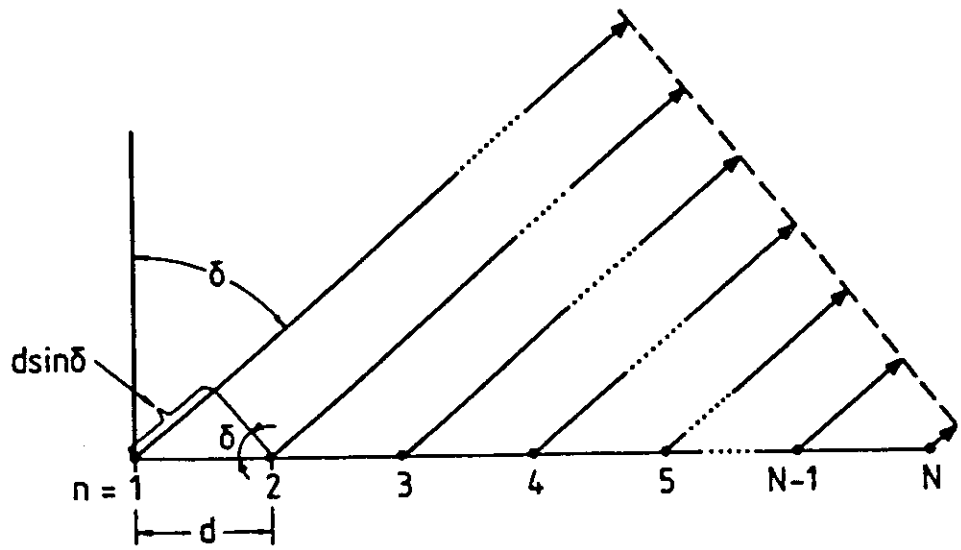

Schematic drawing of wave vectors of a plain wave radiated under a zenith angle δ from N isotropic antenna elements with spacing d.

Using the above given formula, some patterns of a phased array configuration are computed and displayed here.

Left-hand panels: The upper panel shows the grating lobes at $\pm 90°$ zenith angle when the distance (d) between individual antenna elements is equal to the wavelength ($l = \lambda$). The main centre beam, pointing to the zenith, gets narrower with increasing number of individual elements N. The lower panel shows the pattern when it is tapered (weighted) with the individual element pattern.

Right-hand panels: The upper panel shows the increasing number of grating lobes when the distance between the individual elements is enlarged. The lower panel shows how these grating lobes can be suppressed by increased tapering of the array.

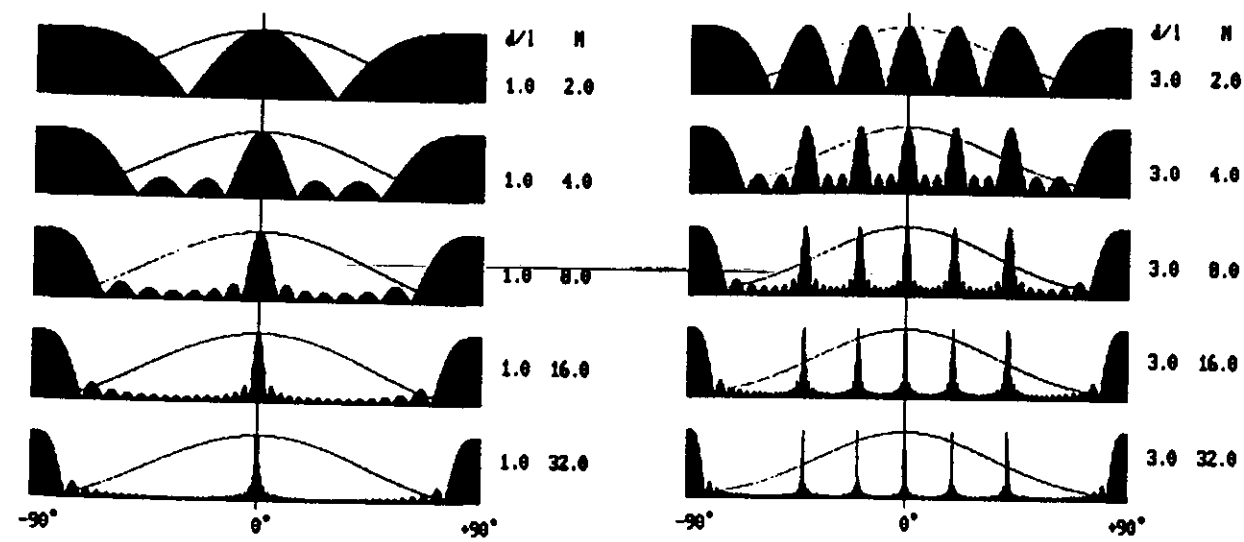

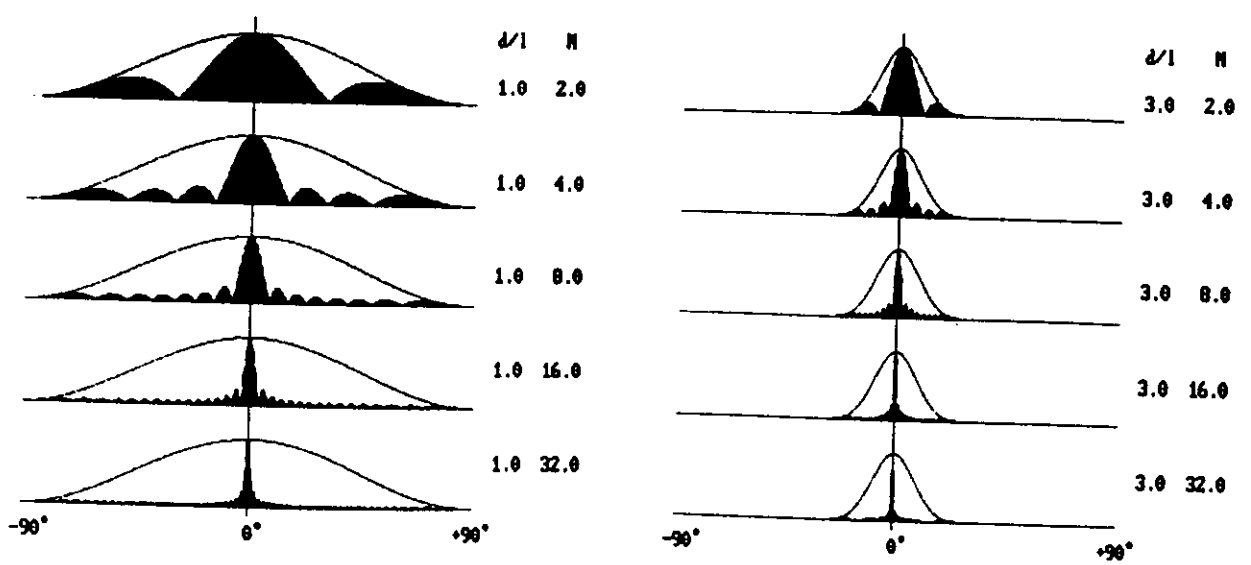

Here we summarize some more parameters of an antenna system, such as effective area, gain tapering and extension into two dimensions.

The antenna pattern, particularly the desired variation of the direction δ_o of the main lobe, can be changed by applying a linearly progressing phase Φ_n from element to element, which has to be $\Phi_n = 2\pi d(n-1)\sin\delta_o/\Pi_o$. This beam steering should be within reasonable limits of the individual element pattern $E_n(\delta)$ to avoid undesirable degrading of the antenna radiation. Furthermore the effective area of an antenna, which is fixed on the ground, is reduced with larger zenith angles because the illumination changes by $\sin\delta$.

To obtain improved sidelobe suppressions, a tapering of the antenna array can be applied by either changing the weighting function W_n (electrical weighting, i.e. feeding the outer elements of an array with less power than the inner elements), or by using unequal element spacings d_n (spatial weighting, i.e. applying larger spacings for the outer elements of an antenna array). The price one has to pay for the improvement of sidelobe suppression by tapering is always a broadening of the main lobe and lowering of the antenna gain G. Using a triangular weighting, for instance, improves the one-way suppression of the first sidelobe to -26 dB, but widens the main lobe by a factor of 1.44 and reduces the gain by 25%, as compared to uniform weighting. The respective values for a $\cos^2$-weighting, which is a good approximation to a Gaussian weighting, are -32 dB, 1.64 and 33%.

These one-dimensional considerations can be extended easily to a realistic two-dimensional radar antenna array by using, instead of d, the projections d' of all element positions onto n axis elongated in the azimuth direction α. The total antenna pattern then can be calculated for any α and δ. For a real radar antenna we also have to consider that the radiation can be into only one half-sphere. For an array system this means that reflections from the ground, a screen or reflector elements have to be included in the calculations. The antenna gain G is defined as the ratio of the maximum radiation intensity (in the main beam) to the average radiation intensity (averaged over all δ and α). For an antenna array with reasonable sidelobe suppression it is proportional to the antenna area and is given approximately by the inverse of the two orthogonal beam widths δ_B' and δ_B'' (in radians):

$$G = \frac{4\pi\ A}{\Pi_o^2} \approx \frac{4\pi}{\delta_B'\delta_B''} . \qquad (4)$$

The effective area A or aperture of the antenna is the product of the physical area of the antenna and the efficiency of its illumination, which for instance may be reduced by tapering. It is noted that A does not include the losses of the antenna elements and its feed system.

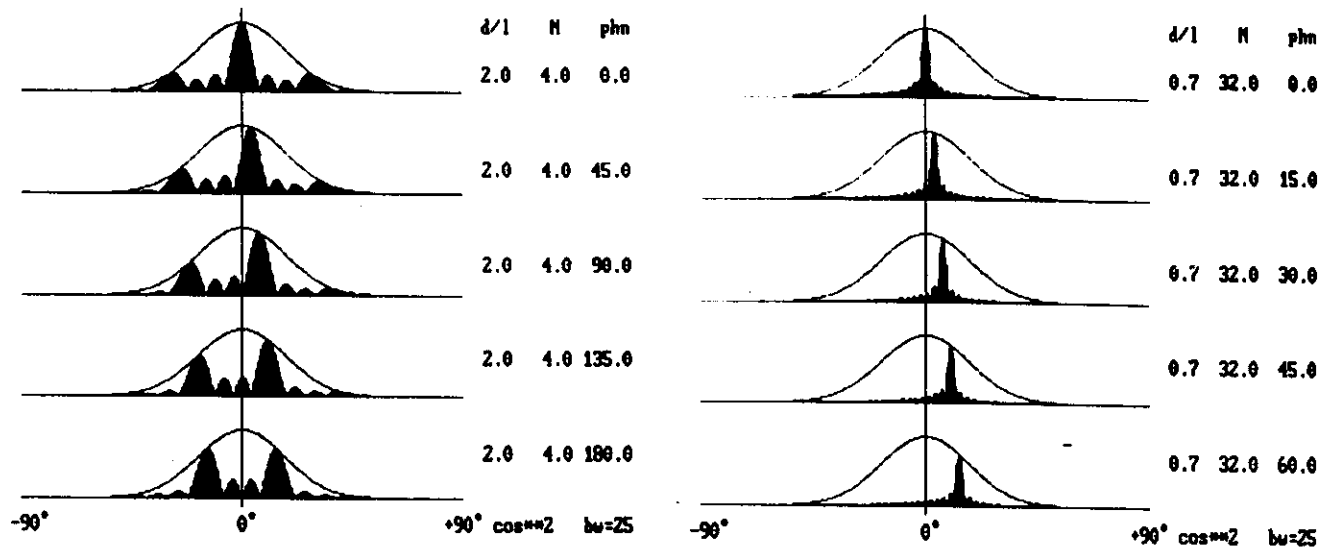

The beam of a phased array can be pointed to different directions by applying a phase difference phn to the individual elements.

The left-hand panel shows this for 4 individual elements, which are separated by two wavelengths. Note that for larger zenith angles when one grating lobe moves away from zenith, the opposite grating lobe moves closer to the zenith. This causes, even when applying tapering, ambiguity for too large zenith angles and has to be avoided by properly choosing the distance between the individual elements or avoiding moving the main beam too far out from zenith.

The right-hand panel shows a properly designed antenna pattern where the beam can be pointed to off-zenith angles without the grating-lobe problem. This is an optimum design for MST radar applications in the interferometer mode where the grating lobe suppression results from the proper distance of the individual elements (d/l = 0.7) for the receiving antenna, and the tapering (given by the solid curve) results from the pattern of the transmitting antenna.

The off-zenith pointing of a receiving array in the right-hand panel can be achieved by electronically adding phase differences to individual elements and it can also be achieved by doing this off-line to the digital data (post-beam-steering). The latter is equivalent to MST radar imaging.

In the interferometer mode any target (i.e. scattering structure) in one of the assorted directions of the main beam would result in a phase difference equivalent to phn. Thus, measuring phn (usually done off-line) yields directly the direction to the scattering target.

In the **radar interferometer** application (SDI) the transmitting antenna illuminates structures in the atmosphere, which scatter the radar signal back to several receiving antennas, where these signals are detected and undergo the interferometer analysis. This means that the transmitting array pattern has to be taken into account in the interpretation.

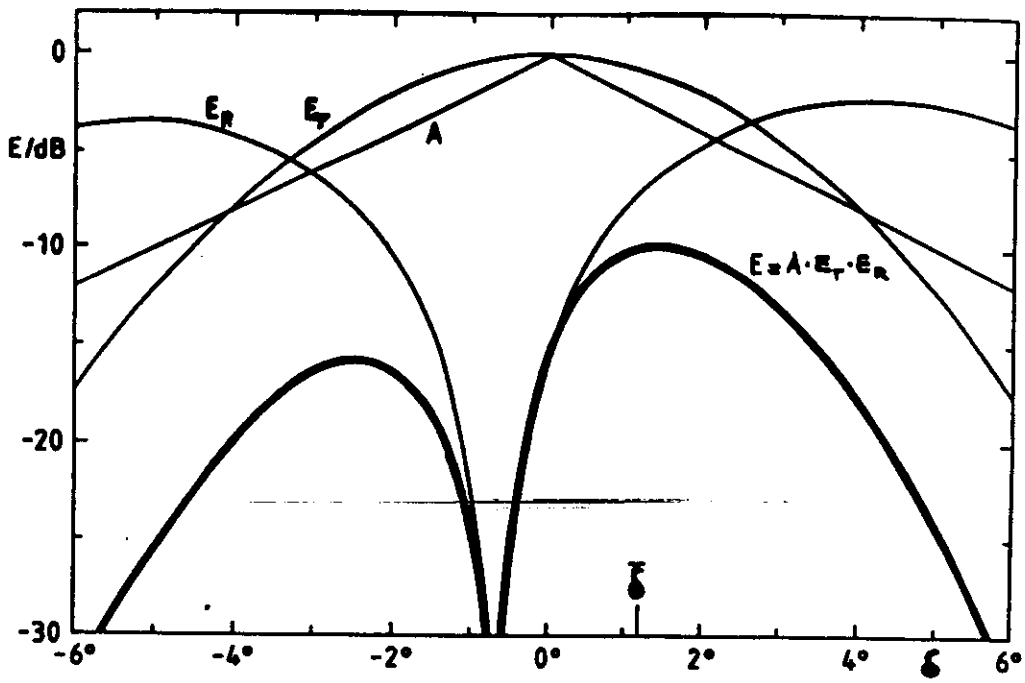

This graph presents a real combination of patterns used in an initial MST radar experiment by Röttger and Ierkic (Radio Science, 1985). It shows the transmitting antenna pattern E_T, the receiving antenna pattern E_R, the assumed aspect sensitivity of a scattering/reflecting MST structure A, and finally the product of these three components, which form the post-set beam E, yielding a mean pointing angle δ. Due to the given receiving antenna configuration, which initially had only two arrays in one direction, the grating lobe shows up on the other side of the zenith.

This method was called **postset-beam-steering (PBS)** and is a zero-order approach of MST radar imaging.

In all contemporary MST radar applications the signals detected at the receiving antenna(s) are digitized and thereafter processed on-line and off-line.

It is absolutely essential that the receiver and the transmitter are **phase-locked** in order to obtain spectral information, and this is highly required also in any interferometer applications. Here it is even more essential that the individual antenna/receiver channels are not only phase-locked (phase-coherent) but also very well calibrated to assure equal phases.

The signals are called to be coherently detected, thereafter they are usually coherently integrated and undergo some further processing as discussed in the following section.

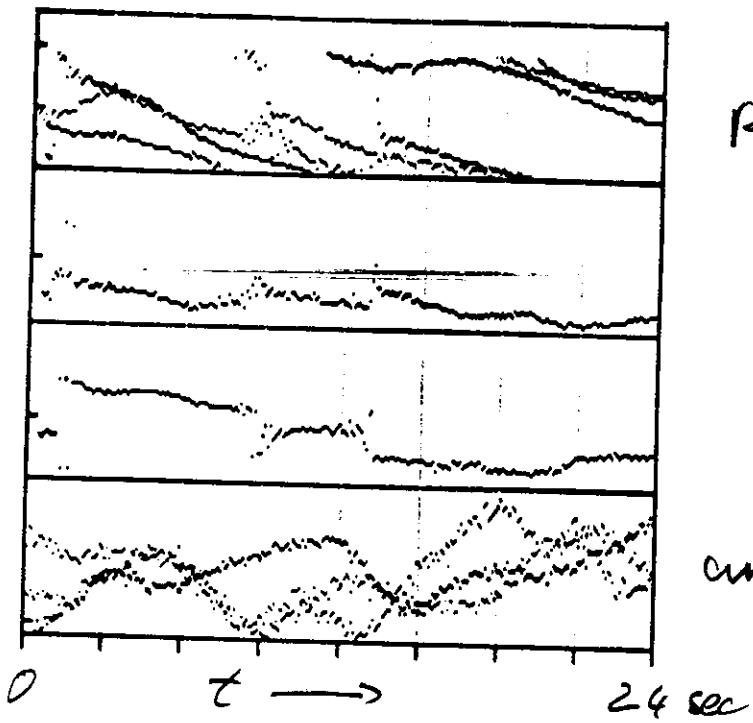

As an example of a real time series we show here the amplitude (lower panel), and the phases (upper panel) of three interferometer channels of MST radar. Usually the so-called quadrature components of these signals are recorded, which is discussed in the following.

(The two centre panels show the zenith and azimuth angles computed from this interferometer set-up; to be discussed later).

Coherent Detection

The oscillator generates a signal s^o at the angular frequency $\Omega_o = 2\pi f_o$ where $f_o = c/\Lambda_o$ is the center radar operation frequency. A pulse train, generated by the radar controller, imposes a modulation to this signal. After amplification in the transmitter (TX in Fig.) the radar signal

$$s(t) = a(t)\exp(i(\Omega_o t + \phi(t)))$$

is transmitted, where $a(t)$ determines an amplitude modulation (by the pulse train) and $\phi(t)$ corresponds to a phase modulation (for coding), and $i = \sqrt{-1}$. $a(t)$ and $\phi(t)$ are slowly varying as compared to $\Omega_o t$. The radar signal is scattered/reflected from the radar volume and reaches the receiver (RX) via the same or a separate antenna. Additionally, noise (sky noise and interference) is received and adds to the radar echo.

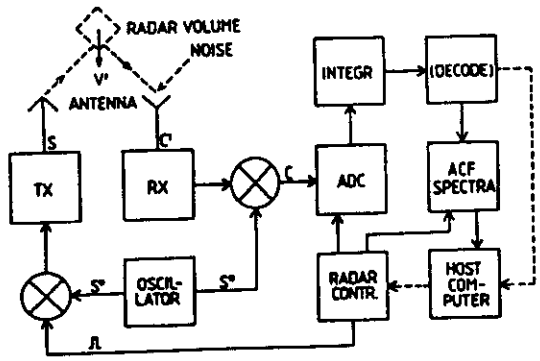

For simplifying the explanation we will assume for a while that the transmitted signal $s(t)$ is not modulated, i.e. $a(t)$=const and $\phi(t)$=const, and the echo results only from a small radar volume at a given range. The echo signal $s'(t)$ plus noise $r(t)$, which are both band-limited because of the scattering process and/or the receiver bandwidth, can be represented by

$$c'(t) = s'(t) + r(t) = a_1(t)\cos \Omega_o t + i a_2(t)\sin \Omega_o t,$$

where $a_1(t)$ and $a_2(t)$ are independent Gaussian variables in a pure scattering process. The uncorrelated noise $r(t)$ contributes only uncertainties to these estimates. After linear amplification in the receiver, $c'(t)$ is coherently detected by multiplicative mixing with s^o. After low-pass or post-detection filtering (to eliminate high frequency components $2\Omega_o$, which are generated during the mixing procedure), this yields

$$c(t) = a^+(t)\cos \theta^+(t) + i a^+(t)\sin \theta^+(t),$$

where

$$a^+(t) = (a_1^2(t) + a_2^2(t))^{1/2}/2. \qquad (6a)$$

$$\theta^+(t) = \arctan (a_2(t)/a_1(t)).$$

The phase $\theta^+(t) = \Omega_D t - \theta'(t)$ is given by the Doppler frequency $\Omega_D = -4\pi V'/\Lambda_o$, which is due to the bulk motion V' of the scatterers. The time variable phase $\theta'(t) = \theta(t) + \phi(t)$, where $\theta(t)$ is caused by the fluctuations of the scatterers-/reflectors in the radar volume. The amplitude $a^+(t)$ is a measure of the reflectivity of the scattering/reflection process. These latter statements are only valid if the noise contributions are separated from the signal. The coherently detected complex signal (+ noise) can be expressed in the form

$$c(t) = x(t) + iy(t), \qquad (6b)$$

where the real part $x(t) = a^+(t)\cos\theta^+(t)$ is called the in-phase component, and the imaginary part $y(t) = a^+(t)\sin\theta^+(t)$ is called the quadrature component. Both components, x and y, are called the quadrature components.

Digital Sampling

We now take into account that the signal c(t) results from scattering and reflection in certain altitude ranges. Frequently these signals which originate from scatter or reflection of a transmitted radar signal are called "radar echoes". We now have to note that the transmitted signal is modulated in order to resolve the range from where the radar echoes arrive from. As sketched in Figs. 1 and 2, the echoes from different ranges then occur at different times at the analog receiver output. In order to allow adapted signal processing of

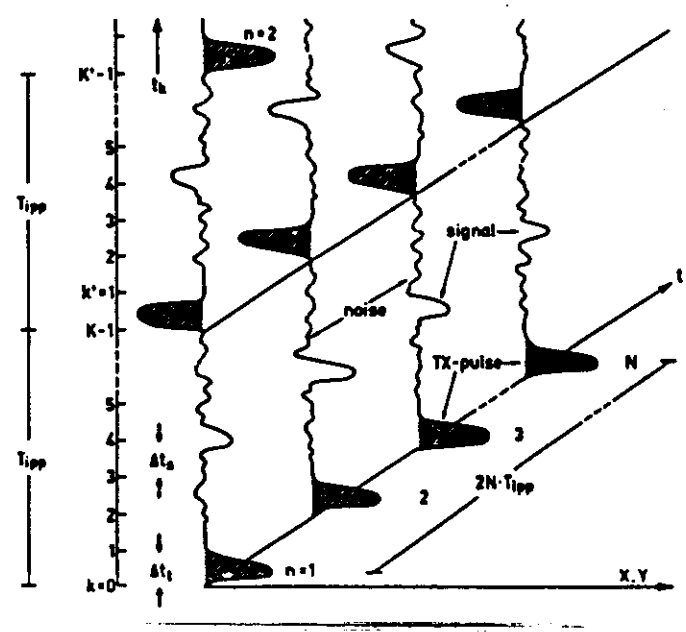

Figure 42. Range-time-amplitude diagram of single-pulse transmitter modulation and coherent MST radar signals.

digitized data, the signal c(t) is sampled at discrete time intervals $t_k = k\delta t_s$ in the analog-digital converter (ADC). This is illustrated in Fig. 42, which shows the amplitude variations of one of the quadrature components of a coherent MST radar signal as they could be monitored with an oscilloscope connected to the output of the postdetection filters, which follow the quadrature detectors. The sequences n = 1,2,... can be assumed to represent successive oscilloscope beam deflections (along the vertical axis), triggered by the leading edge of the transmitter pulse. This pulse is strongly attenuated by receiver gating, as was explained in the last chapter. It is flipped in phase by 180° from one pulse to the next (change from positive to negative amplitude), for the reason of DC-elimination (see details in the following Chapter 4.3). Corresponding to the transmitter-pulse phase ø, the sign of the radar echo also changes from one to the next interpulse period. For convenience the phase of the radar echo is shown here to be similar to the transmitter-pulse phase. The echo phase can take any values, however, depending on the length of the phase path from the transmitter to the radar volume and depending on the relative changes of the scatterers within the radar volume.

On the vertical axis of Fig. 42 the time t_k is given, which directly can be converted to range by means of the definitions of Chapter 1.1. The sampling time interval δt_s should be equal to the radar transmitter pulse length δt_t, since this usually (in case of volume filling scatter) yields an optimum matching to the range gate width or resolution δr. However, in certain cases when narrow reflecting layers shall be resolved, shorter sampling intervals $\delta t^s < \delta t^t$ can be useful; this is called "range oversampling".

The signal and the noise had passed the receiver and postdetection filters and are therefore bandlimited. The response time of the receiver, which is approximately inversely proportional to the filter bandwidth, should also be equal to δt_s, respectively δt_t. The subscript k of t_k is the serial number of the range gate with K = 0,1,..., K-1, where k = 0 corresponds to the beginning or a certain level of the transmitter pulse. Since the quadrature components are digitally sampled, we can write equation (6b) in the form $c_k = x_k + iy_k$. We also call c_k the complex raw data samples.

The number of sampling time steps between successive radar transmitter pulses is K, which is also the number of sampled range gates. The interpulse period is $T_{ipp} = K\,\delta t_s$. The cycle k = 0, ..., K-1 is repeated once with k' = 0, ..., K'-1 with a reversed phase of the transmitter pulse. Both cycles, denoted by k and k' (with k' ≙ k and K' ≙ K), determine one radar cycle $2 \cdot T_{ipp}$ (note that here the radar cycle is two times the interpulse period, because of the introduced phase flip). The serial number of radar cycles is given by n = 1,...,N. One radar burst is determined by N radar cycles, which last for $t_i = 2N \cdot T_{ipp}$. The generation of all pulse trains, needed to control these cycles of the transmitter and receiver-ADC-integrator system,

Coherent Integration and Preprocessing

We will discuss here a standard preprocessing procedure of the pulse-to-pulse technique applied with MST radars. The spectrum which one would obtain for a coherent echo (MST radar) with the sampling rate T_{ipp} is very wide and mostly contains high frequency noise power. The signal power is confined to relatively low frequencies only ($f = 1/\tau_\epsilon \ll 1/2T_{ipp}$), where τ_ϵ is the signal coherence time. It is evident therefore that low pass filtering of a coherent signal, done before the spectrum analysis, will not change the signal characteristics but eliminates high frequency noise contributions. The simplest form of low pass filtering is just the complex addition of the signal + noise samples over an interval $t_i \ll \tau_\epsilon$. A readily noticed effect of such an averaging over N interpulse periods is the reduction of the number of total samples by a factor 1/N. We have to note that this processing step of coherent integration cannot be applied for incoherent signal processing, because the signal coherence time is shorter than the interpulse period. This also means that the described DC- and clutter-elimination is not applicable for incoherent signals. The standard procedure of autocorrelation function and spectrum computation, however, is compatible in both applications.

Since the noise (r) and the signal (s) are independent of each other, their quadrature components add to $c_{kn} = c_{kn}^r + c_{kn}^s$, where c_{kn}^r ($= x_{kn}^r + iy_{kn}^r$) are the quadrature components of the noise and c_{kn}^s those of the signal. A DC-bias can result from a constant, instrumentally introduced voltage at the receiver output c_{kn}^i, or due to radar clutter c_{kn}^c (clutter = echo from a fixed target). All these contributions are additive:

$$c_{kn} = c_{kn}^r + c_{kn}^s + c_{kn}^i + c_{kn}^c.$$

We have to take into account that each radar cycle yields two samples per range gate, namely k and k'. The samples of signal and clutter are shifted by 180° from k to k', because the phase $\phi(t)$ of the transmitter was flipped by 180° (change $\phi(t)$ by 180° in equations (5) and (6)). This can be accounted for by changing the sign of $c_{k'n}$ when averaging

$$c_{k,k'} = \frac{1}{N}\sum_{n=1}^{N}(c_{kn} - c_{k'n})$$

$$= \frac{1}{N}\sum_{n=1}^{N}(c_{kn}^{r} - c_{k'n}^{r} + c_{kn}^{s} - c_{k'n}^{s} + c_{kn}^{i} - c_{k'n}^{i} + c_{knc} - c_{k'nc}).$$

Since for the instrumental DC-bias $c_{kn}^{i} = c_{k'n}^{i}$, it is eliminated by averaging. This is called instrumental-DC elimination (DC = direct current, better to say: constant voltage contribution).

Because of the transmitter phase flip, we find that: $c_{kn}^{s} = -c_{k'n}^{s}$ and $c_{kn}^{c} = -c_{k'n}^{c}$. Since the noise is independent from one to the next interpulse period, a change in sign of c_{kn}^{r} does not change its statistical properties. We thus obtain, since k' = k:

$$c_k = \frac{2}{N}\sum_{n=1}^{N}(c_{kn}^{r} + c_{kn}^{s} + c_{kn}^{c}) \qquad (7)$$

This averaging, commonly called "preintegration" or better "coherent integration", has become a standard process in MST radar operations. It yields coherently integrated data samples c_{kl} (l=1, ...L) at the time

$$t_l = 2\cdot l\cdot N\cdot K\cdot \delta t_s$$

for the coherent integration period $t_i = 2\cdot N\cdot K\cdot \delta t_s = 2\cdot N\cdot T_{ipp}$.

If the summation in equation (7) extends over a time period $t_i = 2\cdot N\cdot T_{ipp}$, which is much longer than δt_s, the high-frequency noise contribution vanishes. For a coherent integration period $t_L = 2\cdot L\cdot N\cdot T_{ipp}$, with (L >>N), which is much longer than τ_ϵ, the signal contribution approaches zero since it is fading in amplitude and phase. Only the clutter contribution

$$c_k^{c} = \frac{1}{L}\sum_{l=1}^{L} c_{kl}$$

remains, since it is constant in amplitude and phase. This can be used to eliminate the clutter component by means of a digital high pass filter operation: $c_{kl} = c_{kl} - c_k^{c}$. This operation is called clutter-DC elimination, and is done after the coherent integration.

For the coherent integration given by equation (7), the number N of added samples has to be selected carefully. It is evident that the integration period has to be much shorter than the typical time scale of signal variations due to the fluctuating scatter process as well as due to the frequency changes resulting from the bulk motions of the scattering or reflecting medium. The advantage is, however, that the processing can be made very efficient since only additions (subtractions) but no multiplication of the raw data series with a weighting function are necessary. It is also required that the real part x and the imaginary part y of the detected signal are correctly in quadrature (orthogonal). Ideally they must be phase-shifted by exactly 90° and must have equal amplitudes on the average, otherwise a distortion of the Doppler spectrum results. Accuracies of less than a few degrees phase difference and less than a few percent amplitude difference are tolerable, however, and can be obtained by proper hardware adjustment.

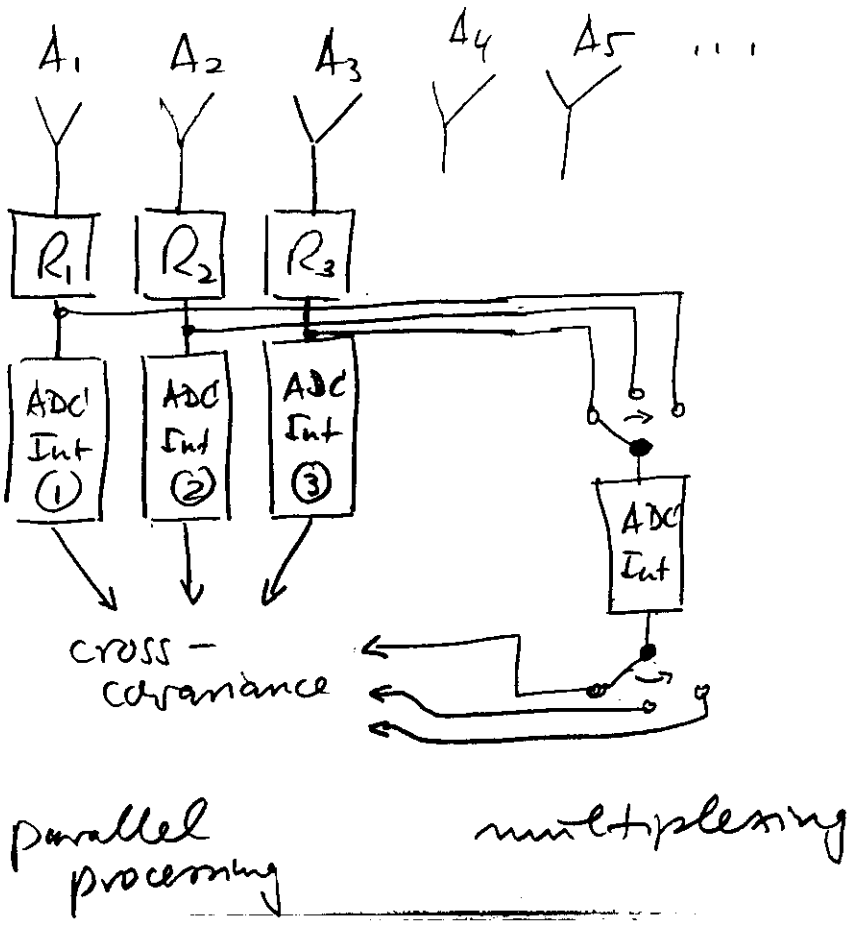

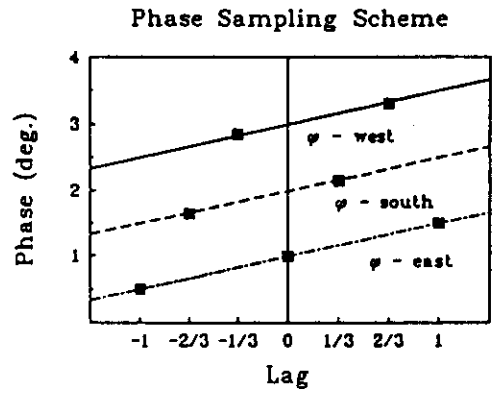

In an optimum interferometer set-up several receiving channels are used to detect signals in parallel, i.e. at exactly the same time. Where such multi-channel possibilities do not exist, multiplexing can be applied, as is shown in this sketch. However, great care has to be taken in the latter case, since the phases of the signals change as function of time due to Doppler shifts. This has to be corrected for as indicated in the lower graph.

From the series of the quadrature components covariance functions and spectra are computed in the following way.

The complex autovariance function of the quadrature components c(t) is

$$g(\tau) = \int c(t)\cdot c^*(t+\tau)dt,$$

where τ is the temporal displacement, and the * denotes the complex conjugate. In digital form

$$R_k(\tau_j) = \frac{1}{L-j}\sum_{l=1}^{L-j} c_{kl}\cdot c^*_{kl+j} = \overline{c_{kl}\cdot c^*_{kl+j}}, \quad \text{with } j=0,\ldots,J-1 \text{ and } J \leq L,$$

where j is the lag index defining the lag τ_j. For a fixed range k, we find $c_l = x_l + iy_l$, and the covariance function becomes

$$R(\tau_j) = (x_l x_{l+j}+y_l y_{l+j}) + i(x_{l+j}y_l - x_l y_{l+j})$$

$$= R_r(\tau_j) + i\, R_i(\tau_j),$$

or $$R(\tau_j) = |R(\tau_j)|\, \exp(i(\tau_j)),$$

with $|R| = (R_r^2+R_i^2)^{\frac{1}{2}}$ and $\phi = \arctan(R_i/R_r)$.

In radar applications the term correlation function is often used for $R(\tau_j)$ instead of covariance function. The correct definition of the correlation function $\varsigma(\tau_j)$ is given by the normalized covariance function:

$$\varsigma(\tau_j) = R(\tau_j)/\, R(0).$$

As well as the autocorrelation function of the series c(t) we also compute cross-correlation functions for two different series, $c_1(t)$ and $c_2(t)$, in the spaced antenna applications and use their modulus in the drift analysis and their phase and amplitude in the interferometer analysis. In a principally similar way also cross spectra are computed from two time series.

The power spectrum is the Fourier transform of $\varsigma(T)$, weighted by W(T):

$$P(\Omega) = \int W(\tau)\cdot\varsigma(\tau)\, \exp(-i\Omega\tau)d\tau$$

or in digital form:

$$P_k(\Omega_m) = \frac{1}{J}\sum_{j=0}^{J-1} W_j\cdot R_{kj}\, \exp(-i\Omega_m j t_l),$$

where W_j is an arbitrary weighting function (e.g., $W_j = J^{-1}$ for all j, etc.) and $\Omega_m = m\,\pi/J \cdot t_l$; $m = 0,\ldots.\, J$. The length of the integration time interval is $t_l = 2\cdot N\cdot T_{ipp}$ in the case of a coherent signal. For an incoherent signal, t_l corresponds to the time interval over which lag samples of the ACF are collected.

The **cross covariance function (CCF)** of two complex series (1,2) is:

$$CCF_k(\tau_j) = (L\text{-}j)^{-1} \Sigma_l^{L-j} c_{1kl} \cdot c^*_{2kl+j} = \langle c_1 \cdot c^*_2 \rangle$$

The Fourier transform is the **cross spectrum**:

$$P_c(\omega_m) = J^{-1} \Sigma_j^{J-1} w_j CCF_{kj} \exp(-i\omega_m j t_i)$$

The normalized cross spectrum is called the **coherence**:

$$Coh\ (\omega_m) = P_{ck}(\omega_m) / (P_{k1}(\omega_m)^{1/2} P_{k2}(\omega_m)^{1/2})$$

Essentially the phase of these complex components is used to determine the angular position of scatterers. The coherence is a measure of angular distribution. This is usually being done as function of the frequency, which will be discussed next.

In an initial approach of the SDI the phase difference can be determined by computing the cross-covariance function of the complex signals, detected at two antennas (note that the symbols for zenith/tilt angles, Θ and δ, are equivalent in this and the following figures). The determination of the cross-covariance function and the effects of the vertical and horizontal velocity will be discussed .

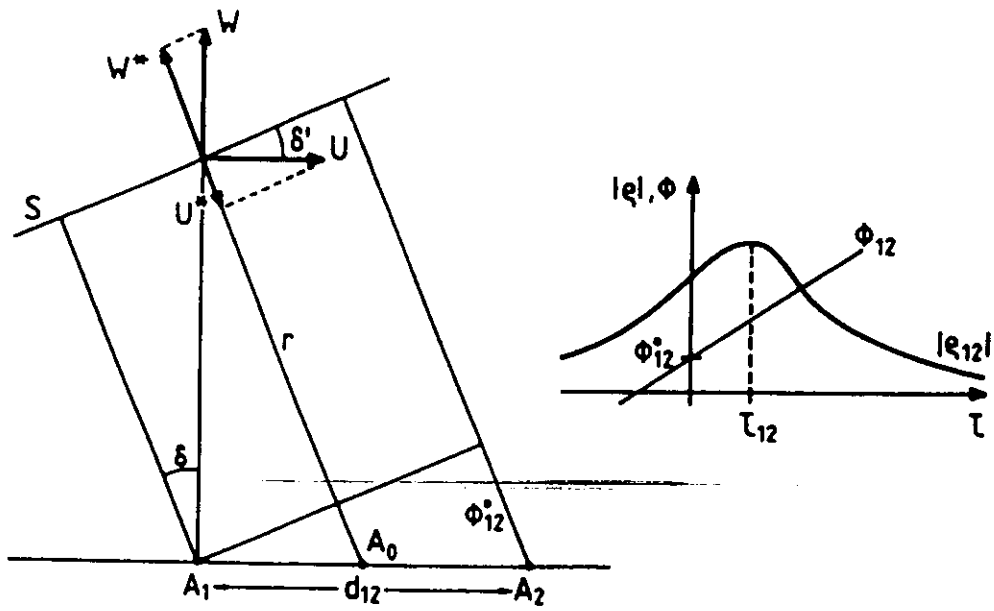

(Left-hand side) Sketch of the geometry of phase measurements of a plane wave reflected from a straight surface S at a distance r from the center A_0 of the radar antennas A_1 and A_2, which are spaced at a distance d_{12}. The surface is inclined with respect to the horizontal at an angle δ' which is equal to the incidence or zenith angle δ. The surface is moving horizontally with the velocity U and vertically with the velocity W, causing the velocity components U^* and W^* in direction of the reflected wave. (Right-hand side) Amplitude $|\rho|$ and phase ϕ of the complex cross-correlation function as a function of temporal lag τ [from *Röttger and Ierkic*, 1985].

This method using the phase of the cross-covariance function at zero lag averages over all Doppler-frequencies. When using just one pair of antennas it yields the apparent direction angle δ (generally called zenith or incidence angle) in the plane determined by the baseline of the two antennas to the mean phase centre of the scattering/reflection region aloft, called reflecting straight surface in the caption of the fore-mentioned graph.

A minimum of three antennas, preferably set-up in an equilateral triangle, is needed to deduce the actual azimuth and the zenith angle. The following graphs shows profiles of several parameters, and in particular the incidence/zenith angle profile (components in E-W and N-S planes).

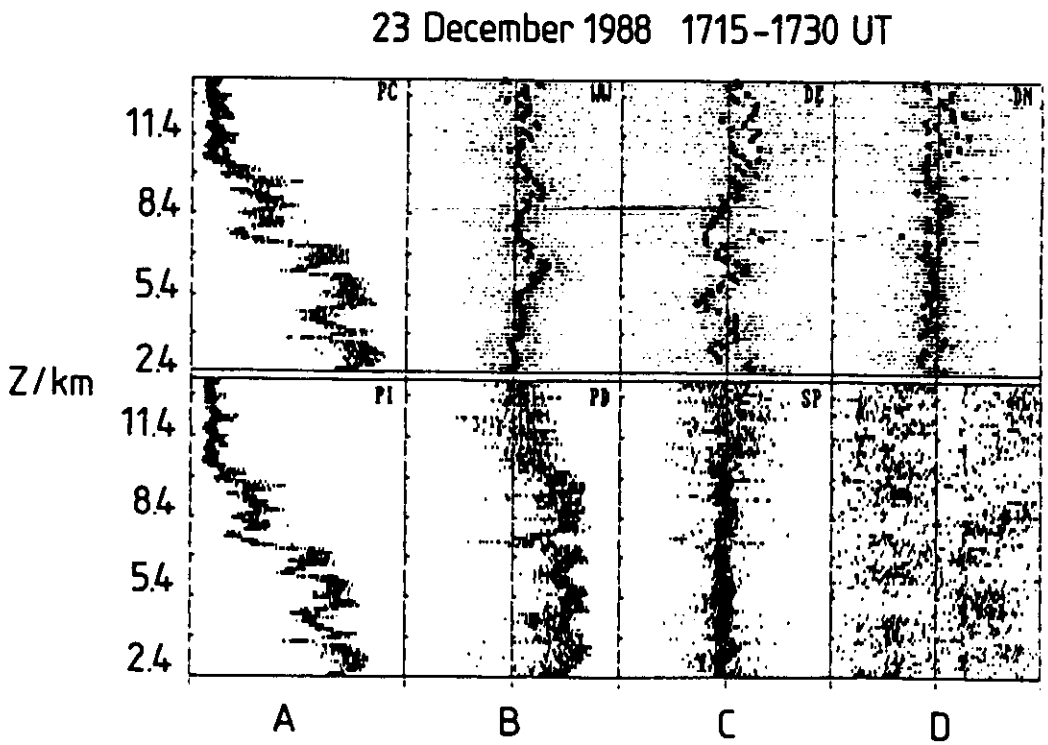

Distribution plots of data taken with the Chung-Li VHF radar on December 19, 1988: (*a*) Power profiles resulting from the coherent addition of signal amplitudes (upper panel, PC) and from the incoherent addition of power (lower panel, PI) received in the three antenna channels. The lower power limit is 0 dB and the upper limit 60 dB. (*b*) Radial velocity (WW) within ± 1 m s^{-1} limits (upper panel), and power difference (PD = PC − PI) within ± 6 dB (lower panel). (*c*) Eastward component (DE) of the incidence angle δ (upper panel) within limits of $\pm 3°$, and the sum (SP) of the phase differences (lower panel) between all three antennas within limits of $\pm \pi$. (*d*) Northward component (DN) of the incidence angle δ (upper panel) within limits of $\pm 3°$, and azimuth direction AL (lower panel) of the incidence vector within limits of $\pm 180°$. The filled squares in the plots 5*b*, 5*c*, and 5*d* of the upper panel indicate the mean values, and the small dots are the single data points acquired within 30 s.

We note in the foregoing graph, that obviously the incidence angle can significantly deviate from the zenith direction. This is interpreted as a tilt or inclination of the scattering/reflecting layer with respect to the horizontal plane. There are implications on the interpretation of the meteorology and the dynamics of the atmosphere, which should not be discussed here. We just enhance the effect this tilt has on the vertical velocity estimates.

In the case of an inclined structure the wave vector of the signal scattered/reflected back to the receiver the velocity component V'_R is measured rather than the real vertical velocity W. There is proof for this, since the tilt and the radial velocity measured are correlated, which indicates that a component of the horizontal velocity is contributing to the radial velocity V'_R.

Measuring also the incidence δ this estimate of the velocity V'_R can be corrected if the horizontal velocity U is known. The latter can be measured with the full-correlation or full-spectrum analysis of the spaced antenna set-up. The vertical velocity then simply becomes:

$$W = (V'_R + U \cdot \sin \delta) / \cos \delta$$

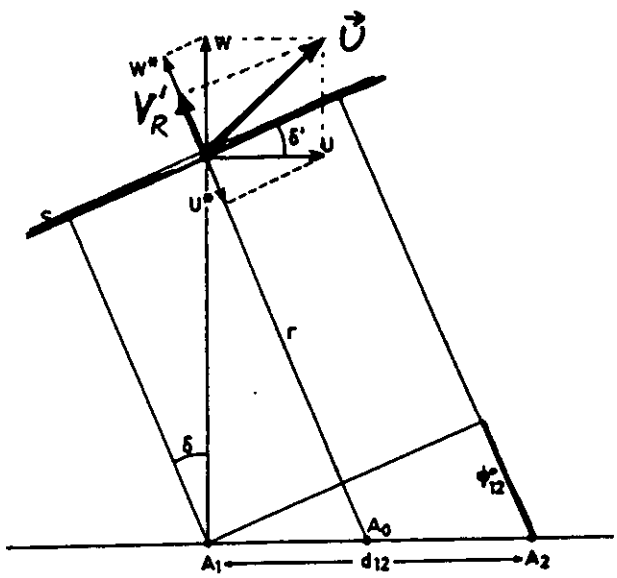

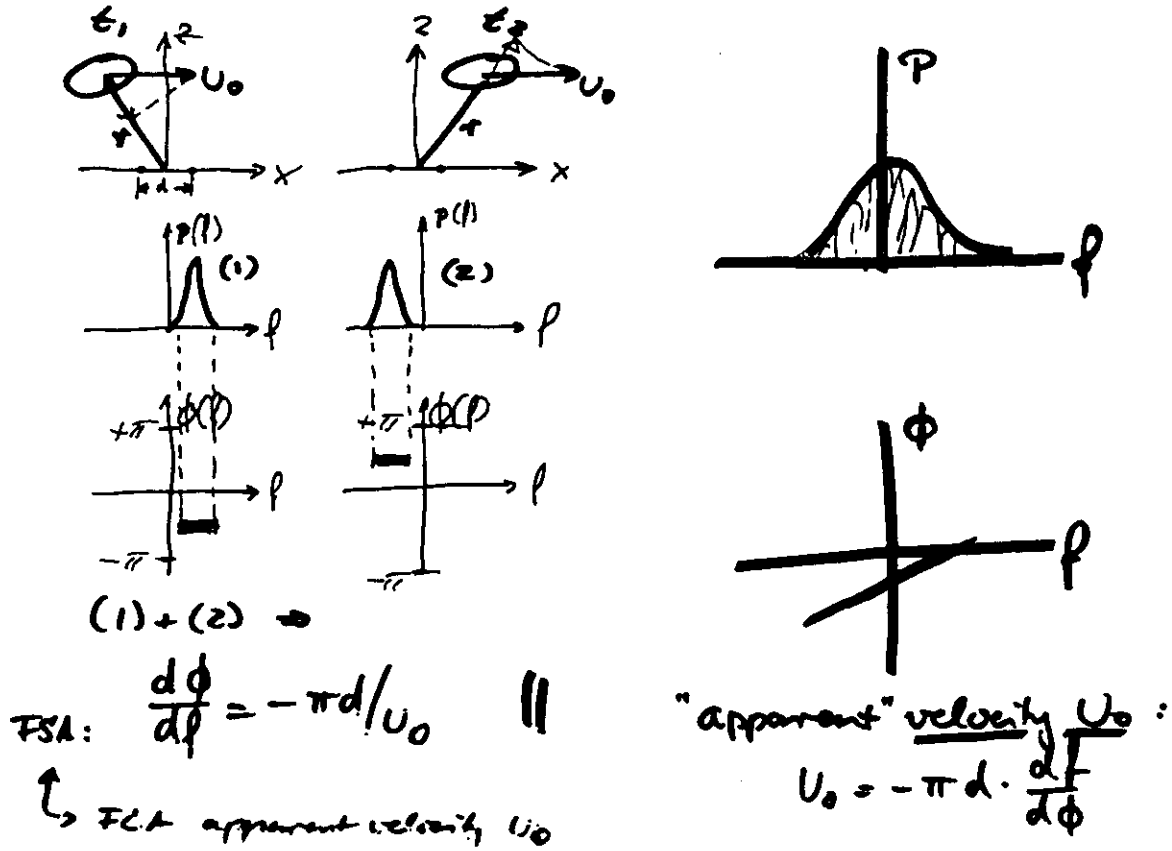

There is of course more information in the data by taking into account the Doppler ferquency. Usually the phase Φ, i.e. the angle δ, is determined as function of the Doppler frequency $\omega = 2\pi f$. Let us now assume, as shown in the upper part of the left-hand-side sketch, that there is a discrete localized target (scattering or reflecting) at range r, which is illuminated by the radar transmitter. This target moves horizontally with velocity U_0. It thus has a velocity component in direction towards the radar when δ is unequal 0. At time t_1 we, thus, determine a positive Doppler shift in the spectrum P(f), and a negative at time t_2. The measured phases Φ are reversed, since the target is located at opposite sides of the zenith at t_1 and t_2. An elementary calculation leads to a simple relation between U_0 and the difference of the phases. All this simplified approach in one dimensions assumes that the vertical velocity is zero and there is also no change in the scatter cross section of the target. In two dimensions, also the cross wind has to be taken into account. For distributed targets, as will be discussed next, the power and the phase of the cross spectrum will schematically look like the sketch in the right-hand panel.

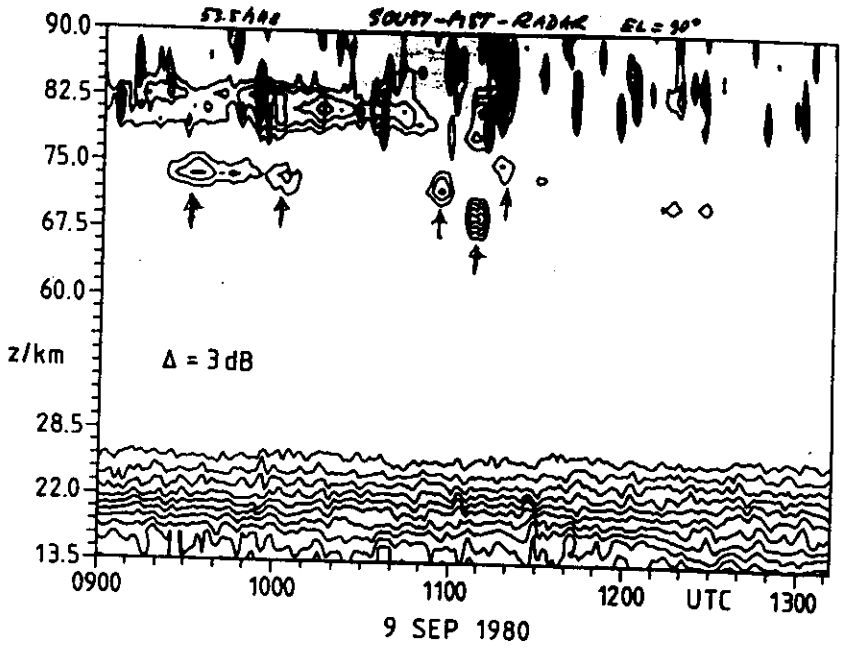

The arrows in this height-time-intensity plot of mesospheric VHF radar echoes indicate structures, which were assumed to be discrete turbulence patches moving through the antenna beam. This could be proved by the corresponding spatial domain interferometer analysis, which showed a change of phase Φ, i.e. incidence angle δ, as function of time.

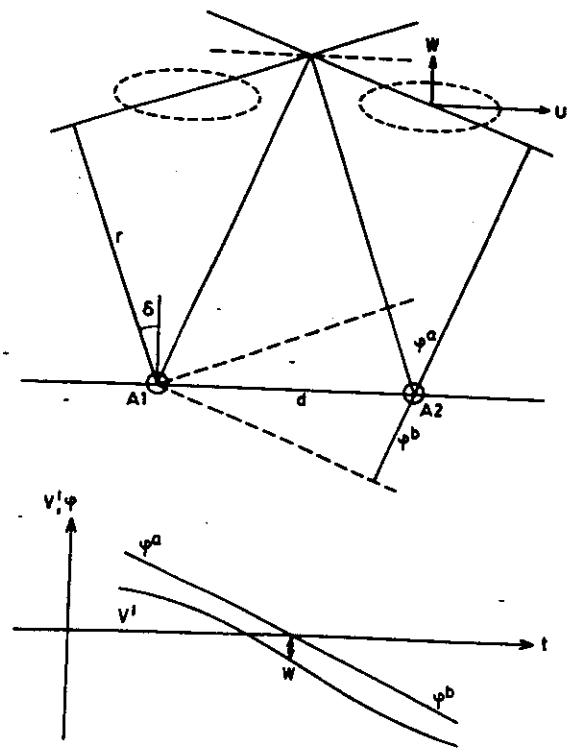

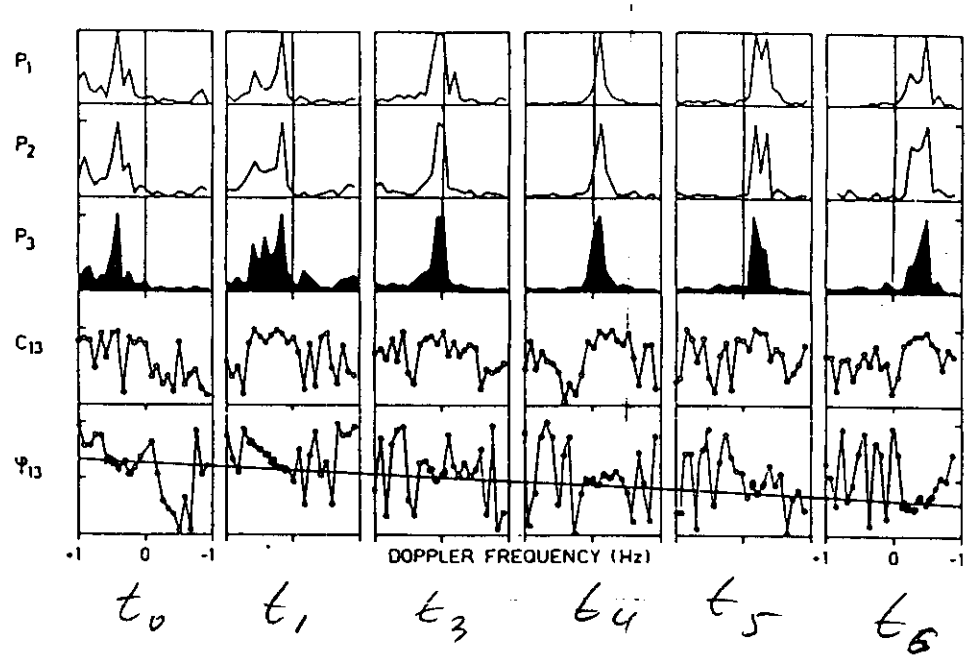

The cross spectra showed significant power at negative frequencies in the beginning, which then moved with time to positive frequencies; in the same period the phase was changing, resulting from changes of the location of the scattering blobs. This is shown in the lower polar diagram (Röttger and Ierkic). The phase also changes internally in the spectra (upper diagram); this phase slope will be discussed next.

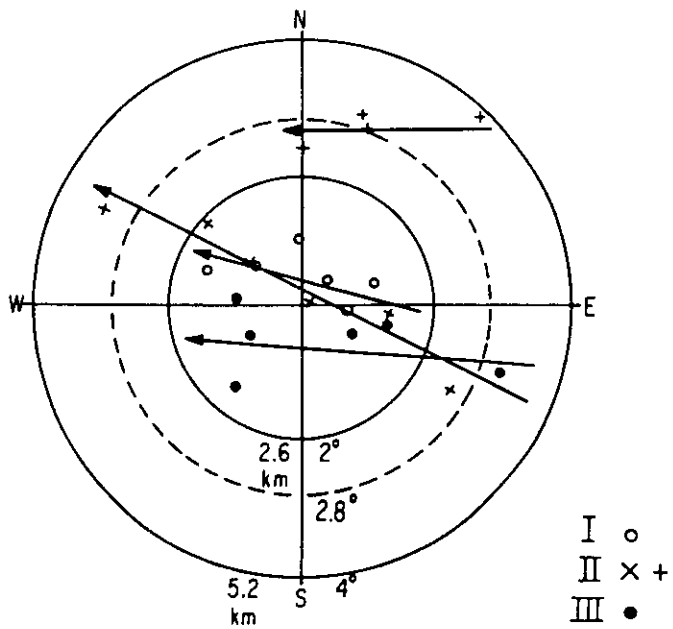

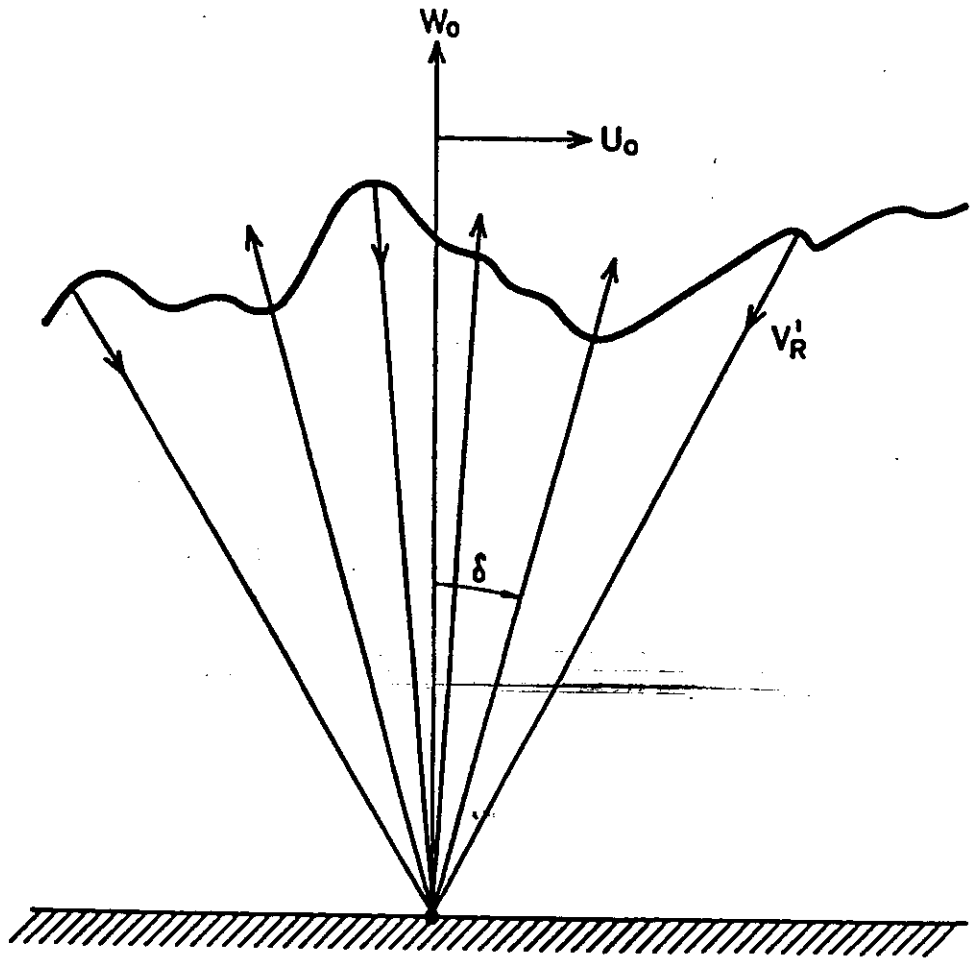

Schematic view of a rough surface of refractive index structure causing several radar echoes reflected back to the origin. Depending on the mean vertical (W_0) and mean horizontal (U_0) velocities as well as intrinsic fluctuating velocities, different radial velocities occur for the different radar echoes from certain sections of the surface.

Here we show a first MST radar cross spectrum in power and phase, where the slope of the phase can clearly be seen. This corresponds to a change of zenith angle δ as function of Doppler frequency f.

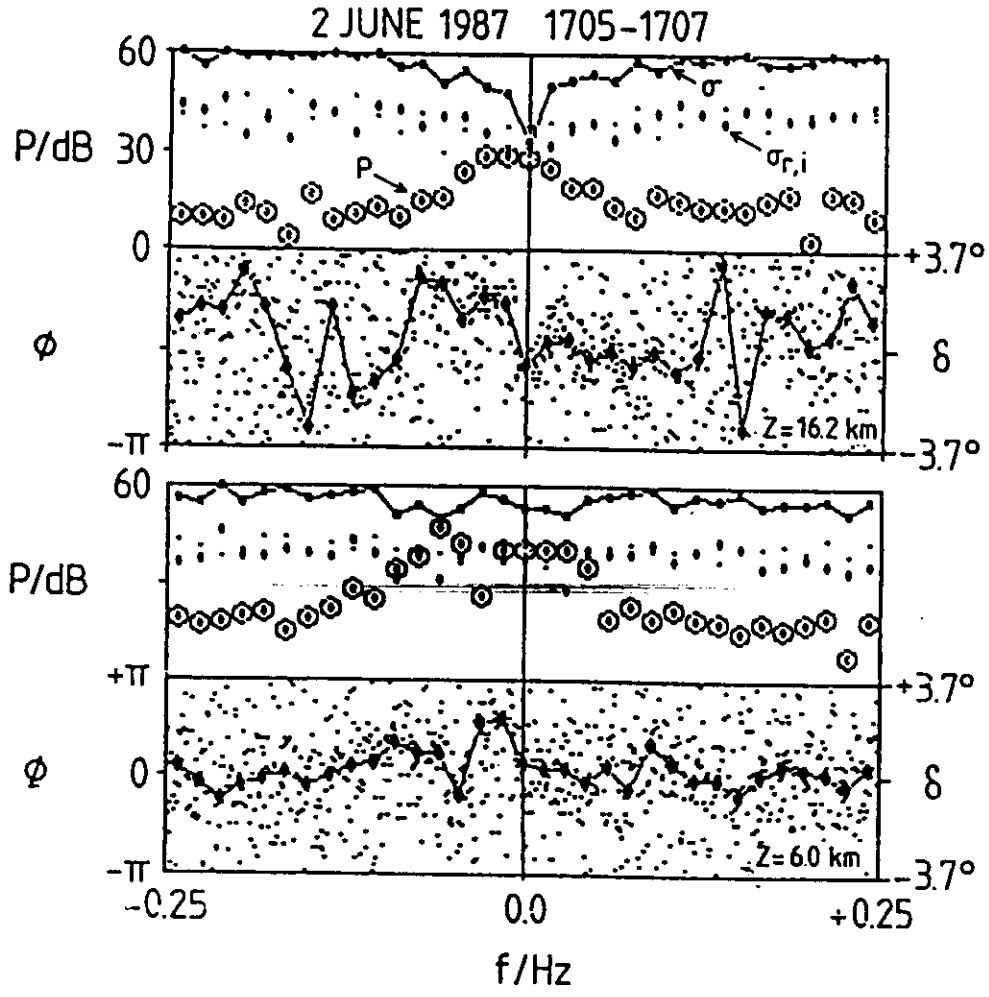

Power spectra P and the phases ϕ of cross spectra of VHF radar echoes from the altitudes z = 16.2 km (upper panels) and 6 km (lower panels), deduced from data taken with the antenna combination 1-2. The term σ denote the normalized variance of the quadrature components of the cross spectra,

A simple computation yields the relation between the slope $d\phi/df$ of the phase in the cross spectrum and the mean horizontal wind speed U_0. The Doppler frequency f resulting from a horizontal wind U_0, measured at an incidence angle δ (see, for instance, the definitions in Figures) is $f = -2U_0 \sin \delta/\lambda$, where λ is the radar wavelength. The phase ϕ between two antennas is given by $\phi = 2\pi d \sin \delta/\lambda$. Combining these two relations and differentiating by f yields the slope:

$$d\phi/df = -\pi d/U_0 \qquad (1)$$

The distance d between the antennas is measured in meters. U_0 in m s^{-1}, ϕ in radians, and f in Hertz. This formula holds for the very simplified assumption of pointlike antennas and a frozen-in refractive index structure moving in direction of the antenna baseline. Equation (1), using this primitive model, which is basically consistent with the more comprehensive equation (29) of *Liu et al.* [1990], already allows us to explain the observed phase slope of the cross spectra to be caused by the horizontal wind. It thus also allows us to estimate the mean wind speed from the phase slope

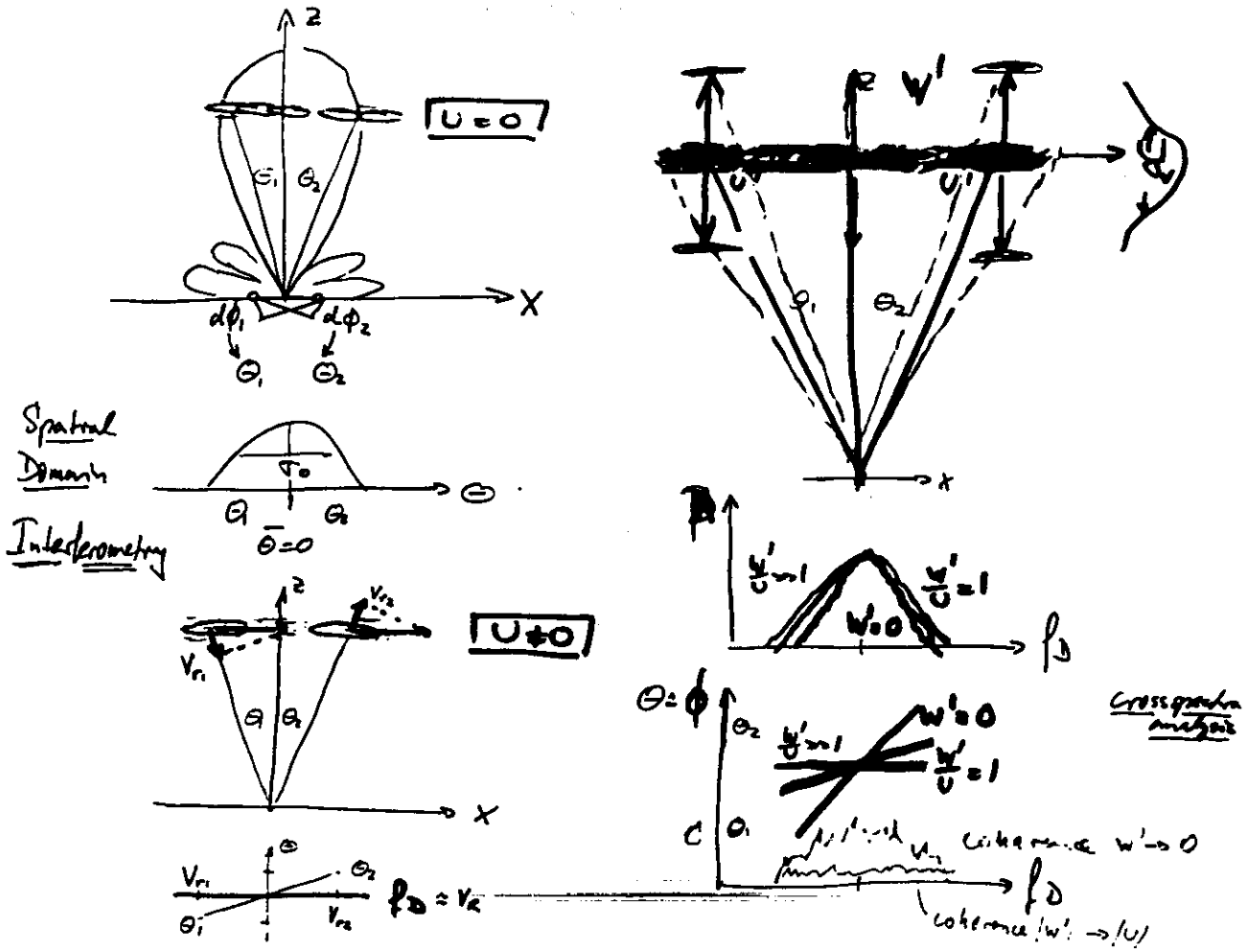

For a distributed target, i.e. a scattering in the atmosphere, which fills the radar beam (transmitting and receiving), the power P as function of zenith angle Θ ($=\delta$) can be assumed to be as shown in the left-hand panel. For fully isotropic scattering this distribution is directly given by the antenna beam pattern. For anisotropic scatter or partial reflection from a rough surface, which is anisotropic, too, the distribution is the product of the angular distribution and the antenna pattern.

When the distributed target moves horizontally, the velocity (i.e. the Doppler frequency) changes as function of Φ (i.e. δ). When the layer has some internal random velocity variations u' and w', as shown in the right-hand panel, the power spectrum gets broader, the coherence gets smaller and the slope dΦ/df gets shallower. This needs to be considered carefully in the analysis of the data, and has been theoretically treated by Liu et al. and Doviak et al.

The method just demonstrated in its basics is called the full spectrum analysis (FSA). It is the Doppler frequency domain counterpart of the full correlation analysis (FCA) of the traditional spaced antenna (SA) method. Both procedures are applied to measure the horizontal wind velocity as well as turbulent velocity by using a spaced antenna system, as displayed in the following diagram. Here also the other method to measure wind velocity, the Doppler-beam-swinging (DBS) technique is sketched, although it is not an interferometer technique. However, the oblique spaced antenna method (OSA) uses interferometer information. These latter methods with fixed off-zenith beam-pointing will not be discussed in this lecture, but can be found in some of the references.

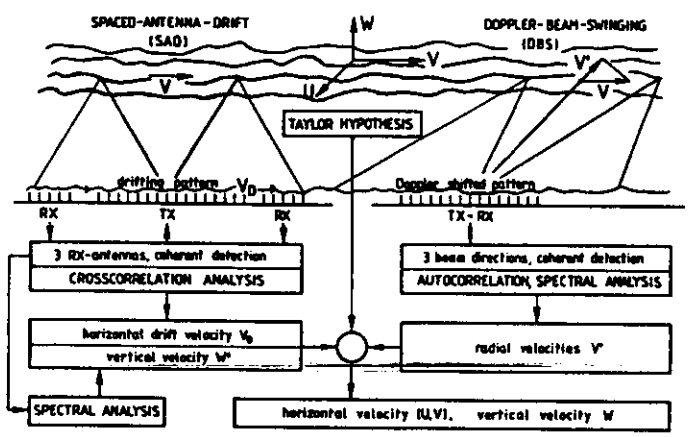

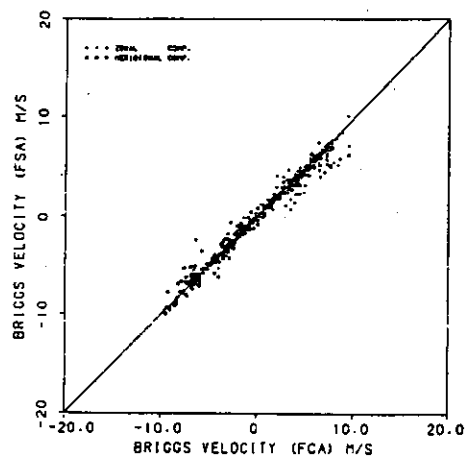

This graph shows that the results applying the full-correlation analysis (FCA) and the full-spectrum analysis (FSA) are well correlated (Pan and Liu).

Interferometry has been applied for radar studies of the troposphere, stratosphere and the mesosphere. After we had in the beginning displayed a few examples of FDI studies of the so-called polar mesosphere summer echoes (PMSE), which show dedicated fine-structure and dynamics, we will now present examples of PMSE SDI. These were obtained with the EISCAT VHF radar in Tromsø, Norway, which allows 2-channel interferometry.

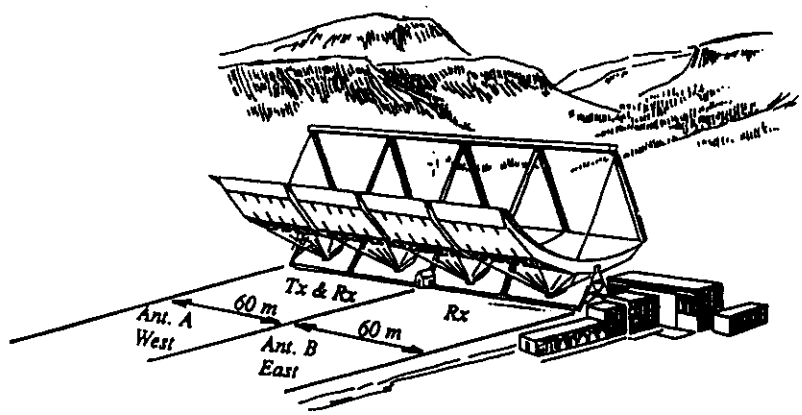

EISCAT VHF antenna: Interferometer configuration.

PMSE are often deformed heavily by waves which can break into turbulence by the Kelvin-Helmholtz instability. Such an event is shown in the following height-time intensity plot and the dynamic spectra (spectrogram) in one range gate in the middle of this breaking layer. The turbulence breaking occurs after 09:40 when the layer had been dramatically lifted up and down by the instability. The double-channel recording of this event allowed an SDI analysis, as shown on the next page.

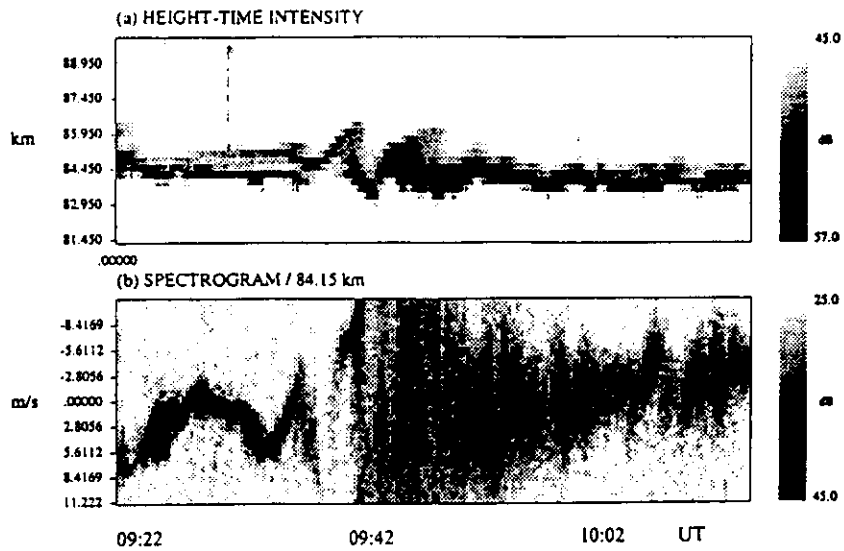

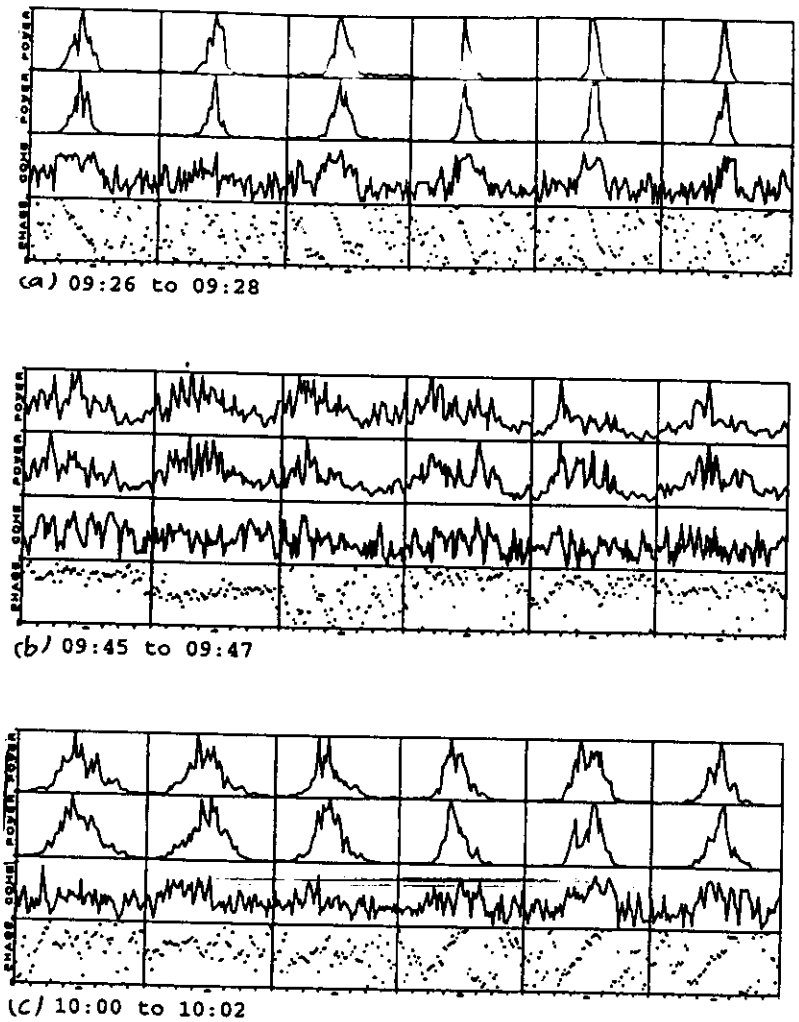

SDI measurements of PMSE: Power spectra of the two channels (upper two sub-panels), coherence (third sub-panels) and phase (lower sub-panels) of the cross spectra of PMSE signals in the range gate 84.15 km (see lower diagram of the previous page). The upper panel (a) shows spectra before the wave breaking, the centre panel (b) during the instability event when turbulence is generated, and the lower panel (c) during the decay phase of the created turbulence. A downward phase slope and significant coherence is clearly visible in the beginning (a), a shallow slope and low coherence when its heavily turbulent (b), and an upward slope and increased coherence (c) during the turbulence decay. The change in phase slope is an obvious sign of total reversal of the horizontal wind velocity, a so-called wind-corner.

How to compute the cross spectrum,
and what does it basically really mean
in terms of interferometry to obtain a radar image of
scattering/reflecting structures in the atmosphere ?

Spatial Domain Interferometry (SDI):

For simplicity we describe the process just for two antennas, which are set up in the horizontal plane along the x-axes. We are also using the notation (Σ rather than $\int$) to comply with digital processing.

The signal voltage at antenna m is:

$$S_m = \Sigma_l A_l(\omega) \exp (j\Phi_l + j\omega t)_m$$

Φ_l is the phase angle and
A_l is the corresponding amplitude of scatterer l

The angular frequency ω results from the bulk radial velocity of the observed scatterers.

The Fourier transform of S_m is:

$$F_m = \Sigma_l A_l(\omega) \exp (j\Phi_l - jkx_m\Theta_l)$$

$k = 2\pi/\lambda$ is the radar wavenumber
x_m is coordinate of the mean phase centre of the antenna m

If it can be assumed that Φ_l are independent of each other, and randomly uniformly distributed between 0 and 2π, then for 2 antennas m,n:

$$<F_m(\omega)\, F^*_n(\omega)> = <\Sigma_l A_l^2 \exp (jk(x_m - x_n)\Theta_l)>_\omega$$

$<>$ is an average over a suitable time period
Θ = sin Θ can be assumed for small Θ

The complex normalized cross spectrum is:

$$C_{m,n}(\omega) = \frac{\langle F_m(\omega)\, F^*_n(\omega)\rangle}{\langle |F_m(\omega)|^2\rangle^{1/2}\, \langle |F_n(\omega)|^2\rangle^{1/2}}$$

For suitable assumptions of distributions of Θ we get:

$$C_{m,n}(\omega) = \exp(-\tfrac{1}{2} k^2 (x_m - x_n)^2 \sigma^2)\, \exp(jk(x_m - x_n)\Theta)_\omega$$

The phase angles as function ω of this cross spectrum is determined by the bulk velocity, as discussed beforehand, and the amplitude, i.e. the coherence, is determined by the angular spread (variance) σ of the scattering layer with mean angular position Θ in horizontal direction.

Frequency Domain Interferometry (FDI):

In a similar way the cross covariance and cross spectra can be obtained for two operating frequencies. This method can principally be extended to an infinite number of frequencies; however, this will soon get close to the equivalent application of widening the transmitter pulse spectrun by narrowing the pulse length, which is obviously also increasing the vertical resolution. There is consequently a trade-off between using FDI and short (coded) pulses.

$$S_{m,n}(\omega) = \exp(-(k_m - k_n)^2 \sigma^2)\, \exp(j2(k_m - k_n) z_w)_\omega$$

m,n = determines the transmitted frequencies
z = the range, i.e. (vertical) position of the layer
σ = the width (vertical thickness) of the layer

Note that FDI determines parameters in direction of (parallel to, usually vertical) the radar wave vector and the SDI orthogonal to the radar wave vector.

MST Radar Imaging

Whereas the previous explanations referred to a set-up of two or (a few more) spaced antennas for SDI and two (or a few more) operating frequencies for FDI, which simply yields only the first moments of the distribution of scatterers or glints on a partially reflecting rough surface, the radar imaging allows full determination of the distributions and consequently their higher order moments of the sensed structure.

Assume that we would be able to have a very large number of receiving antennas at positions x and y, located on a horizontal plane at z = 0. With these antennas we sample the pattern of the electromagnetic field, resulting from scattering or reflection of a transmitted radar signal from an atmospheric structure aloft. We then will obtain the average power:

$$P = \langle |S(x,y,t)|^2 \rangle = 1/2\pi \langle P(\Theta_x, \Theta_y, \omega) \rangle$$

where the averages $\langle\ \rangle$ are over all x, y, t and Θ_x, Θ_y, ω, respectively,
Θ_x, Θ_y are the direction cosines of the elementary angles to the sensed structure.

A so-called **brightness distribution** of the sensed structure is defined as (following radio astronomy):

$$b\ (\Theta_x, \Theta_y, \omega) = P(\Theta_x, \Theta_y, \omega) / P$$

There is also the so-called visibility function, which is the Fourier transform of b, and basically determines the apparent 'visibility' of the scattered signal on ground.

The first moments of b are the mean angular Doppler frequency [ω], the mean of the angles [Θ] in the x-, and in the y-directions, as determined with the 3 antennas. The same procedure, as described in space, can be applied on many operating frequencies; this would finally lead to a three-dimensional brightness distribution.

However, the hardware and software load for such a venture would be tremendous.

The described methods of radar imaging rely on ensemble averaging and assume certain statistical properties of the scattering/reflecting medium. We found that this condition is not always guaranteed in MST radar sounding of the lower and middle atmosphere, as we will show in the following.

A different possibility of imaging the structures aloft is to use the minimum set-up for a spatial domain interferometer, namely three receiving antennas. A range profile of coherent samples, taken at these three antennas of each coherent integration period, is used to calculate the angle of arrival, and its x- and y-components for each range gate r. An ensemble averaging will not be done here but the positions x, y of each single sample will be displayed successively in time for for fixed range in a polar plot. The organization of these single positions gives an indication of the structure image and its persistent or random distribution. One can say, that here the assumption of space-time ergodicity applies.

The following graph shows the basic geometry to calculate these positions. It is assumed, for simplicity, that these radar targets are in the far-field of the radar system and that the determined point-position is equivalent to the location of the mean phase center of the structure, as detected by the MST radar set-up.

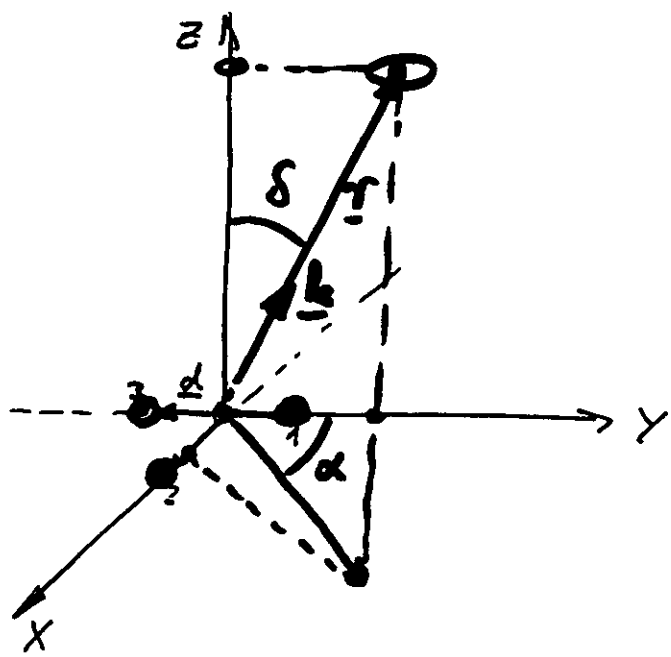

Basing on the configuration on the previous page, placing the mean phase centre of antenna 3 in the origin and all 3 antennas at $z = 0$, and then measuring the phases Φ at the 3 antennas displaced at equal distances d, we obtain the mean positions of the scattering/reflecting centers in x-y coordinates at the range r:

$$x = r \cdot (\Phi_1 - \Phi_3) / kd$$

$$y = r \cdot ((\Phi_1 - \Phi_3) + 2(\Phi_2 - \Phi_3)) / kd\sqrt{3}$$

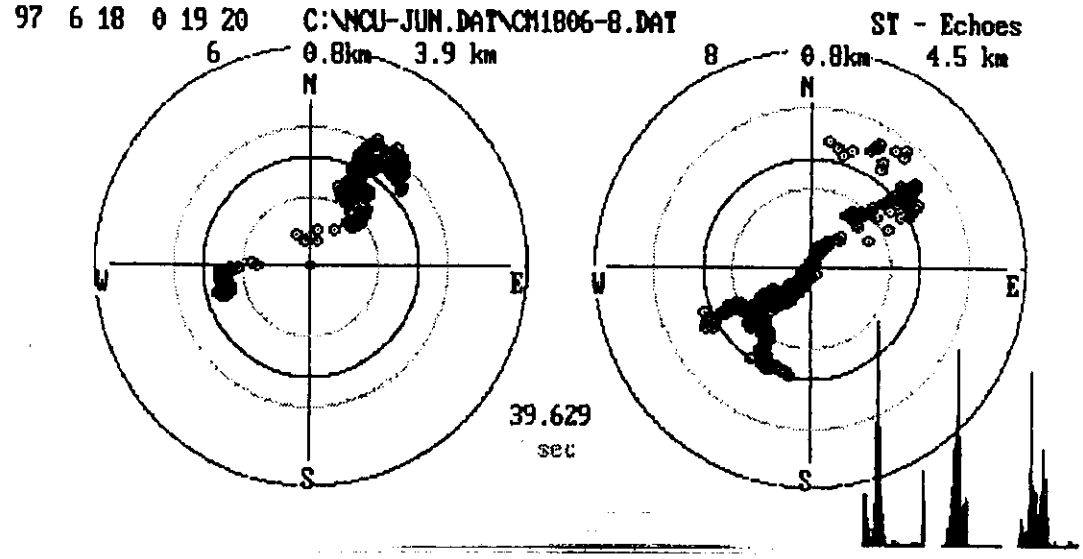

The figure shows the variations of the locations of the phase centers of radar illuminated tropospheric structures in polar coordinates. Each single position point was obtained from 3-antenna complex data sets, recorded (after coherent integration) within 102 ms. The left-hand graph is for range gate 3.9 km and the right-hand for 4.5 km. The circles with center vertically over the radar cover a maximum radius of 0.8 km; the inner ones (in grey) encompass the half-power and first null of the transmitter beam. In the lower right-hand corner the distributions of the phases in range 3.9 km, measured at the 3 antennas, are plotted. The total period of these displays covers 39.6 s. It is recognized that the positions are not randomly scattered, as it would be required for a radar image processing as described before, but show a persistent change in position. We regard these kinds of instantaneous position displays, when adding the power of each single position, as a zero-order brightness distribution, which is regarded quite appropriate for these interferometer applications of MST radar. However, it does not allow suitable estimates of the instantaneous angular frequency. (More explanations of these analyses will be presented at the mst8 workshop).

The just described method was originally developed for interferometry of VHF radar echoes from lightning strokes observed, since the lightning echoes are very transient and endure only for some 100 ms. The following range-time-intensity plot and the range-power profile shows an example of a lightning echo. The lower graphs display the position plots in two range gates as well as the phase distributions and amplitude variations as function of time.

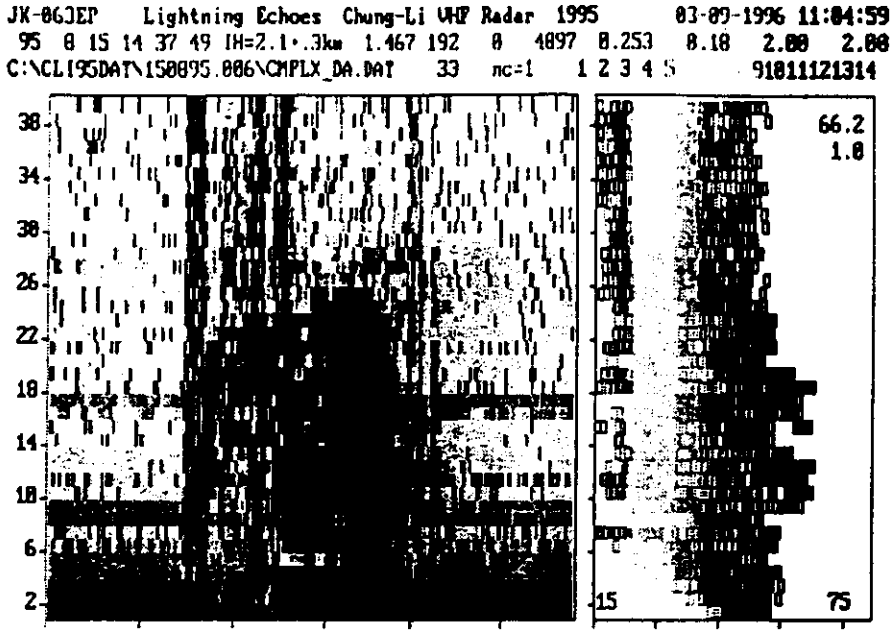

Fig. 1 Range-time-intensity plot (left) and power distribution profile (right) of a radar echo from a lightning stroke observed at 14:37:49 LT on 15 Aug. 1995. The ranges extends over distances from 2.1 km to 13.8 km, and the time axis covers an interval of 1.467 sec (tick marks: 0.253 s). The scale of the power distribution profile covers 15 dB to 75 dB; it also presents the grey-scale used in the RTI plot.

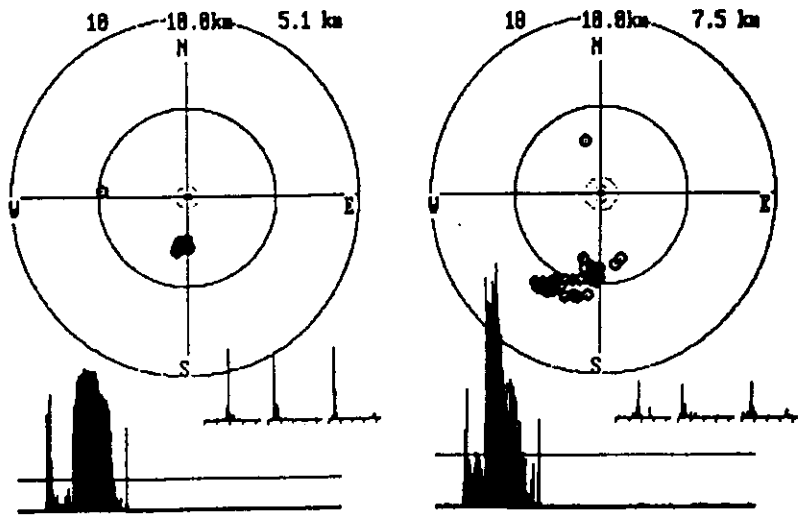

Fig. 2 Polar plots (in geographic directions N-E-S-W) of the positions, the amplitude variation (lower series) and phase distributions (0° - 360° in the three receiver channels) of lightning echoes in the range gates 10 and 18 at distances of 5.1 km and 7.5 km, respectively, corresponding to the lightning stroke shown in Fig. 1.

Knowing the range gate from the sampling time (this is only a coarse estimate; a better choice would be to use FDI for this purpose), the positions of the scattering/reflection points on the lightning channel can be determined, and projected into the 2 orthogonal vertical planes x-z and y-z for the total time of the short event.

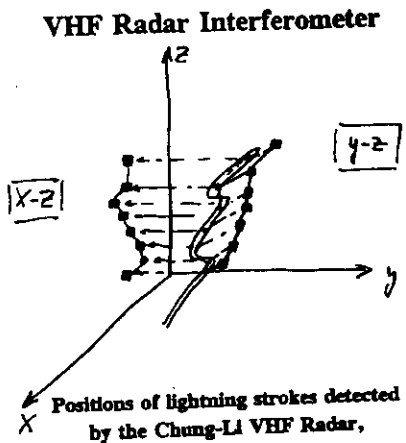

Positions of lightning strokes detected by the Chung-Li VHF Radar, projected into the north-south and the west-east vertical planes

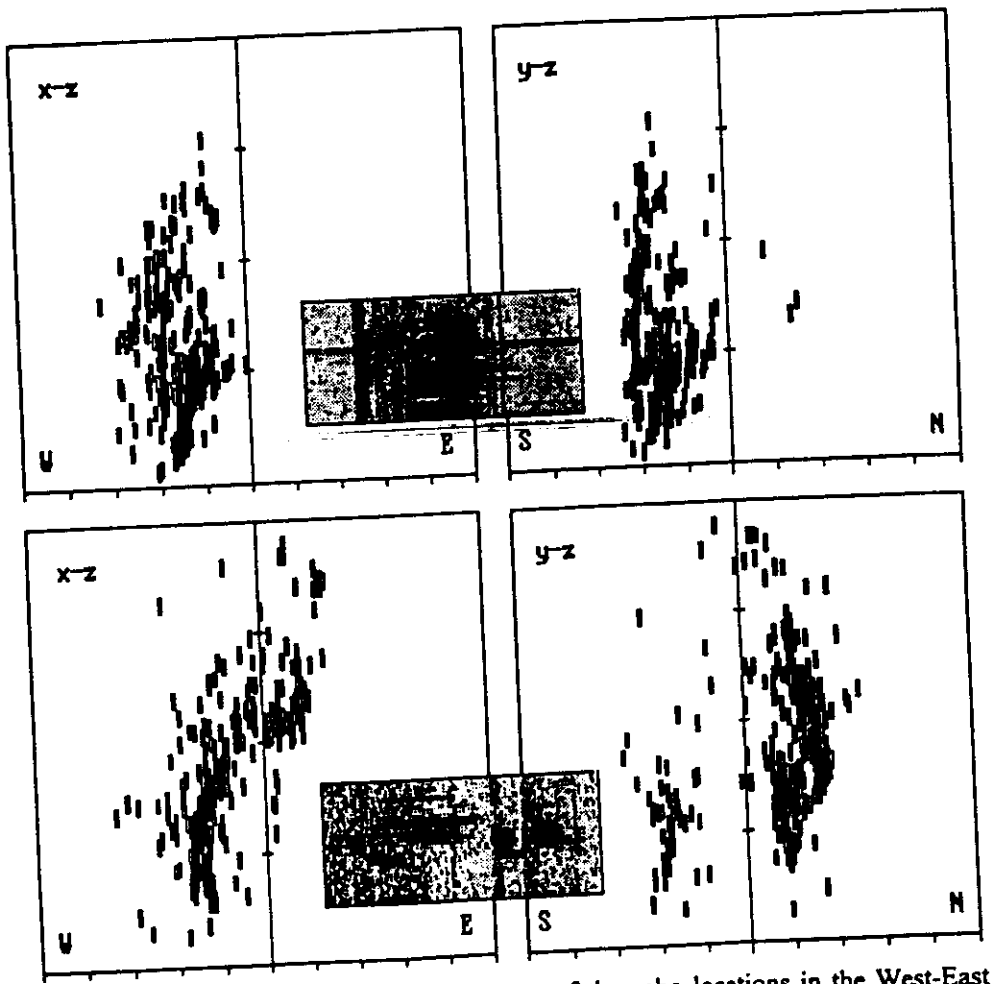

Fig. 3 Radar Displays of Lightning: Plots of the echo locations in the West-East (x-z) and North-South (y-z) planes. The upper plots are for the lightning stroke displayed in Fig. 1, and the lower plot shows a display of another lightning stroke observed at 16:13:08 LT during a thunderstorm on 13 August 1995. The total scale coverage on the horizontal axes is ± 12.5 km (the center line is at the radar location) and 10 km on the vertical axes. The insets show the corresponding range-time-intensity plots for total time intervals of 820 ms.

By determining the positions over some longer time periods than done in the previous plots, the Doppler velocity in radial direction of each of these phase centers can be computed. These can be assumed to be glints on a rough surface, which moves with the mean background wind. This method was introduced by Adams et al. and was called Imaging Doppler Interferometry. The figure shows the position of such glints in the mesosphere, observed with MF radar. From a sufficient number of glints the mean horizontal and vertical velocity can be determined. This is a complementary method to the cross correlation and cross spectra analyses to obtain the wind velocity.

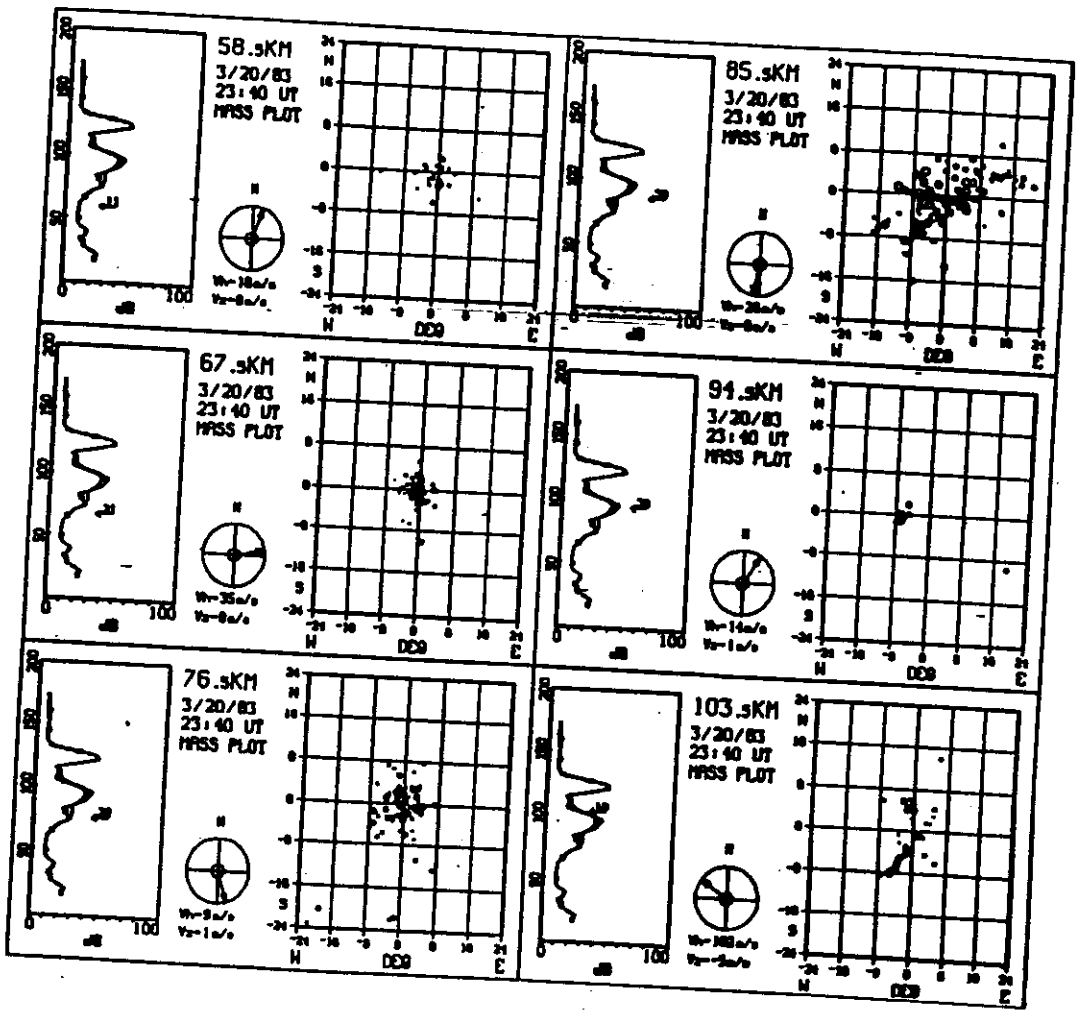

Adams et al. (1985)

Post Beam Steering (PBS)
(Digital Beam Forming)

Assume we have a sufficiently large number of m receiving antennas. The signal voltage detected at each of these antennas is:

$$S_m = A_m(\omega) \exp(j\omega t)$$

By applying suitable phase delays $\Delta\varphi_m$ to each antenna channel the antenna beam can be steered into divers directions when adding the complex voltages from the channels:

$$< S > = \Sigma_m S_m(\Delta\varphi_m)$$

This is done after the complex signals of each channel have been digitized and has been originally called postset-beam-steering (Röttger and Ierkic), it then has become known as post-beam-steering (PBS). It is equivalent to digital beam forming. Compared to electronic beam steering, where the beam pointing is fixed (preset) during transmission and reception, this method has the great advantage that the beam steering is done off-line in any direction within the angular section illuminated by the transmitter beam.

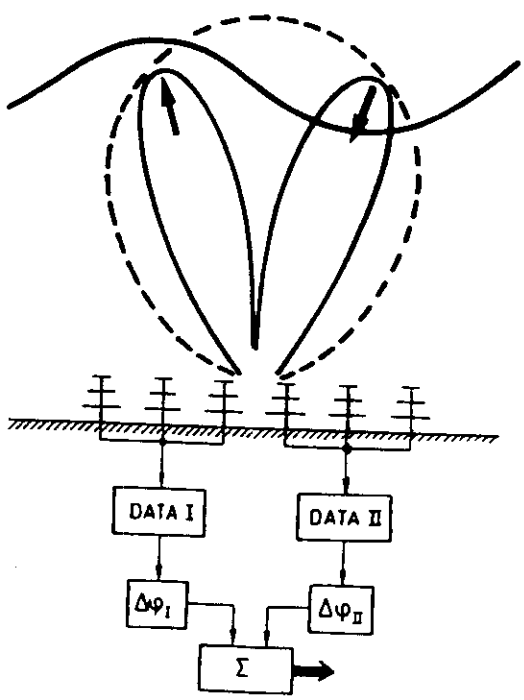

Here we show some results from initial PBS observations, such the lower stratospheric wind velocity and the determination of the full set of gravity wave parameters:

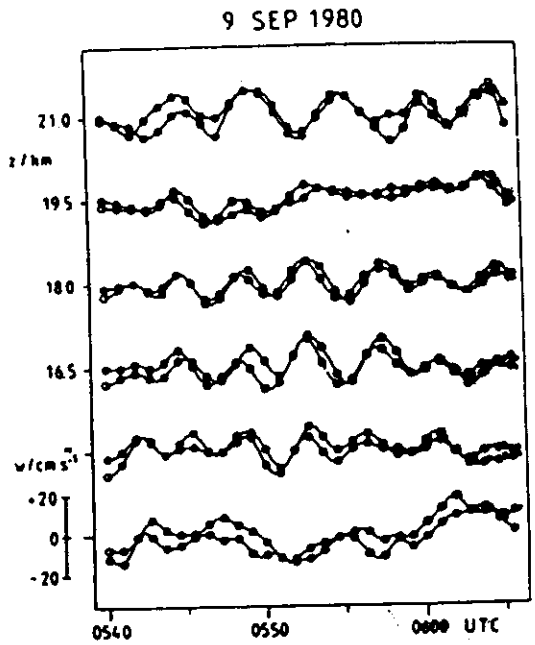

Fig. 8.1b Time series of radial velocity measured with beam tilted to 1.2° north and 1.2° south of zenith (from Röttger and Ierkic, 1985).

CONCLUSIONS:

- **Verification of atmospheric gravity waves**
- **(Intrinsic) wave period ~ 5 min (~ constant with height)**
- **Horizontal wavelength ~10-15 km**
- **Vertical wavelength ~40-50 km**
- **Horizontal phase speed ~40 ms^{-1} and propagation direction 20° E, about constant with height.**
- **Matching the wind velocity in the lower stratosphere shear region (likely the source region)**
- **Atmospheric gravity waves propagate upwards to the middle stratosphere**
- **Vertical fluid velocity due to waves increases exponentially with height to about 15 cm s^{-1} at 22 km**

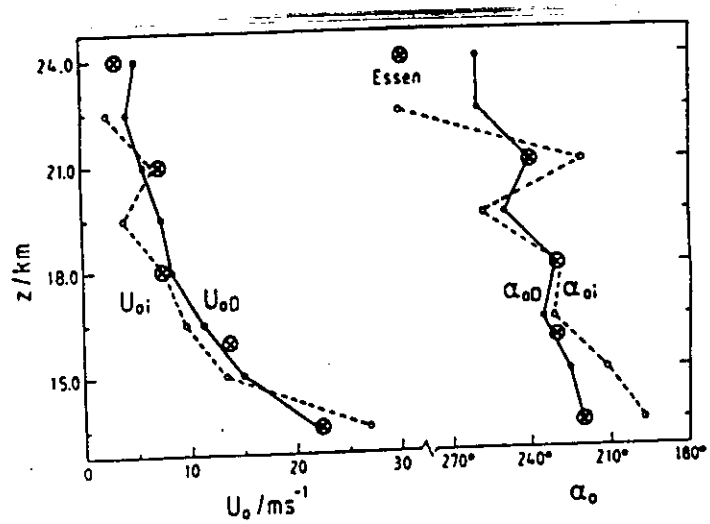

Average wind speed U_0 and direction α_0 measured with the postset beam i and the spaced antenna drift method D, compared with radiosonde data from Essen (circled crosses).

The Fourier transform of S_m is F_m. It was shown by Woodman and Kudeki that the phase delays $\Delta\varphi_m$ can be included into the complex spectra F_m after post-integration, rather than to the initial data time series. This method is called **post-statistics beam-steering (PSS)**. It reduces the computational load, but is basically equivalent to PBS.

It was very obvious already from the first observations of tropospheric and stratospheric VHF radar echoes that there is a pronounced aspect sensitivity (also called angular spectrum). Some advantages and caveats were recognized early, such as the apparent radar beam pointing, as is shown in the following graph. This in particular affects the measurements with the Doppler-beam-swing method (DBS).

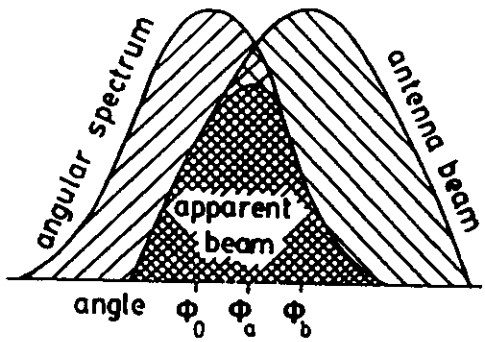

FIG. 9. Sketch showing the effect of the echo enhancement at vertical or near-vertical incidence on the effective pointing angle of a broad antenna beam. The main contribution to the received signal comes from an angle closer to vertical than would be assumed based on the pointing direction for the main beam. In the figure ϕ_0 is the zenith direction, ϕ_b is the real beam direction, and ϕ_a is the apparent beam direction. (After Röttger 1981).

A proper means of obtaining the angular spectrum is either by measuring the brightness distribution, or applying the PBS method in scanning the beam direction off-line. This was done with the MU radar in Japan by van Baelen et al. The following plots show the contour lines of constant echo power in a fixed range gates, measured with 4 antenna subsets of the MU radar. The arrows indicate the horizontal wind direction.

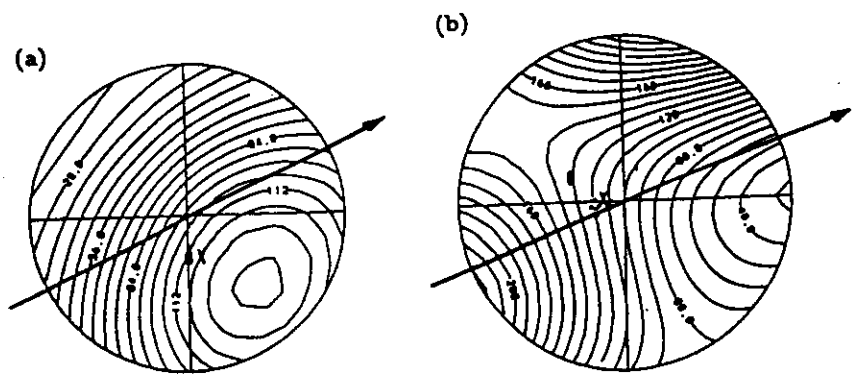

Analysing series of cross spectra we frequently find that the phase is not linearly varying as function of Doppler frequency. The graphs show examples of such events.

RÖTTGER ET AL.: CHUNG-LI VHF RADAR INTERFEROMETER MEASUREMENTS

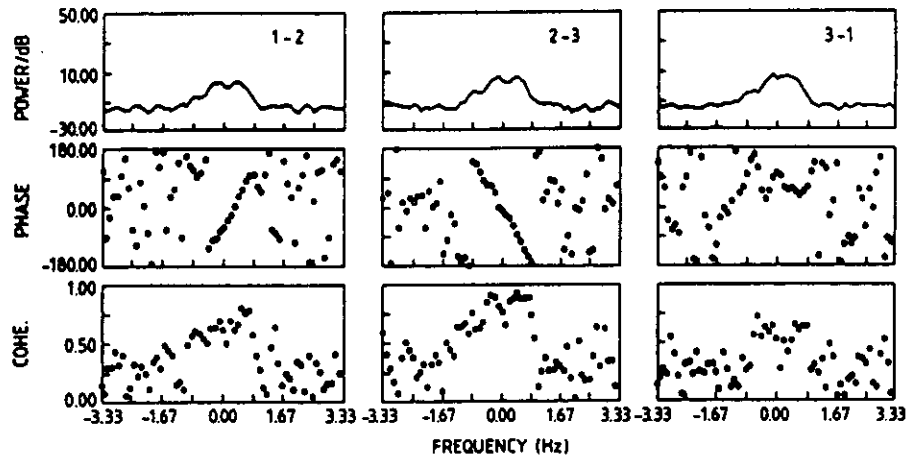

Fig. 3. Power spectra, phase, and coherence of the cross spectra for echoes from 9.4 km altitude measured with the three antenna combinations 1-2, 2-3, and 3-1 on December 9, 1988, at 2325 LT (see *Liu et al.* [this issue] for details).

LIU ET AL.: SPACED ANTENNA MODE FOR MST RADARS 557

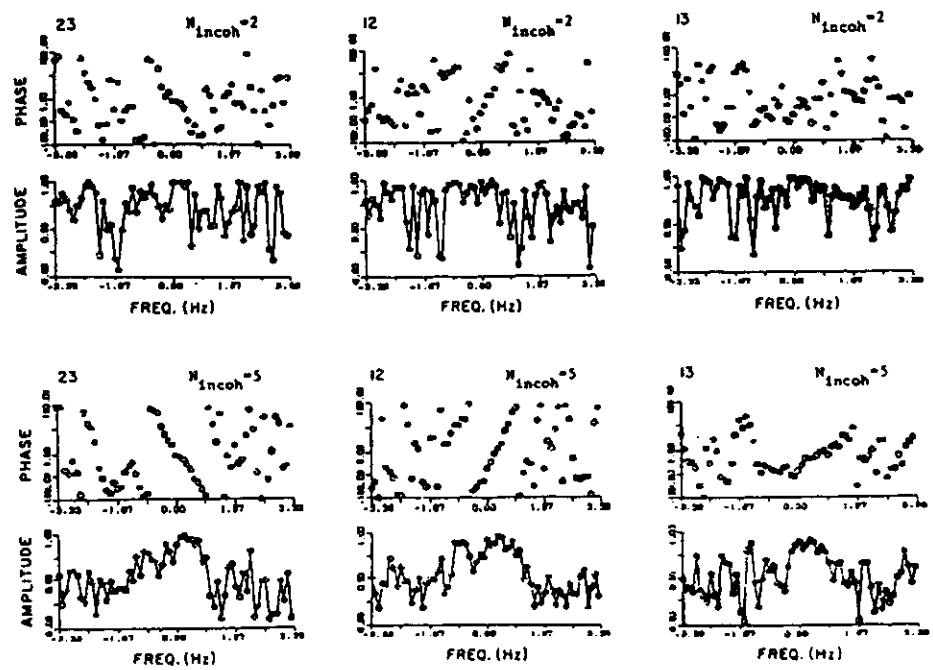

Fig. 5. Examples of observed coherence functions for different N_{incoh}, numbers of incoherent integration. Both phase and amplitude are shown. The vertical scale for the phase is − 180° to + 180°, for amplitude 0 to 1. The horizontal scale is in hertz from − 3.33 to + 3.33.

Such phase variations can occur when the medium is inhomogeneous, either by some non-random changing of the scatter/reflection cross section or layer tilt changes (as seen in the position displays discussed earlier or by differential velocities in the scattering/reflecting medium). The latter is exhibited in the following two graphs, where the horizontal arrows depict wind vectors. The wind field U in left-hand graph is given by $U = \alpha x$, and the right-hand graph by $U = U_0 + \alpha x$. α determines a wind gradient in x-direction, and U_0 is a constant wind. It is immediately seen that depending on position in the radar beam, the horizontal wind vector, and consequently also the projection into the radar wave vector direction changes as function of zenith angle. The Doppler frequency results:

$$\omega_x = -2k \cdot x \cdot (U_0 + \alpha x)/r$$

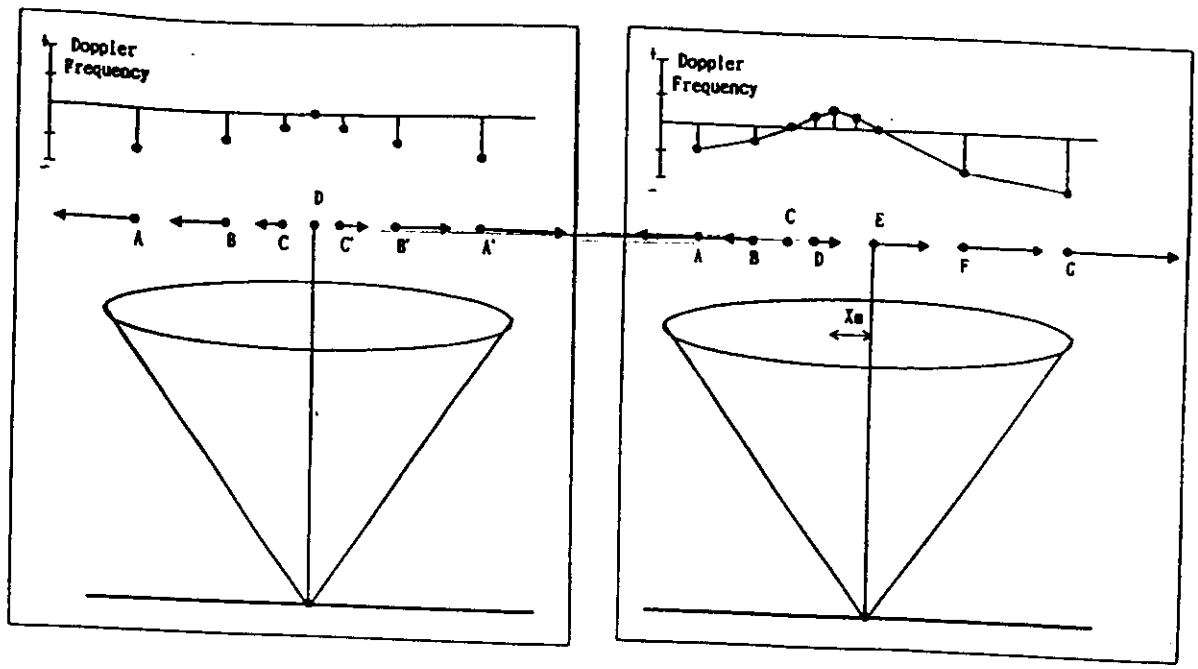

Assuming the basic analysis method to deduce the horizontal wind (i.e. neglecting the curvature of $\Phi(\omega)$) leads to an erroneous velocity estimate:

$$U' = U_0 + \alpha x + \alpha^2 x^2 / U_0$$

Corresponding cross spectra and phases had been calculated and are shown here for ratios G/M, where G is the gradient wind component over the beamwidth and M is the mean wind. We recognize that the phase is no more linear for G/M > 0. It can get highly distorted when the gradient wind is about equal to the mean wind. These effects have to be considered carefully in any analysis using this technique. However, the advantage of this interferometer application is, that we have found a method to check the events for validity of the basic assumptions, governing the entire set of statistical methods described in this lecture.

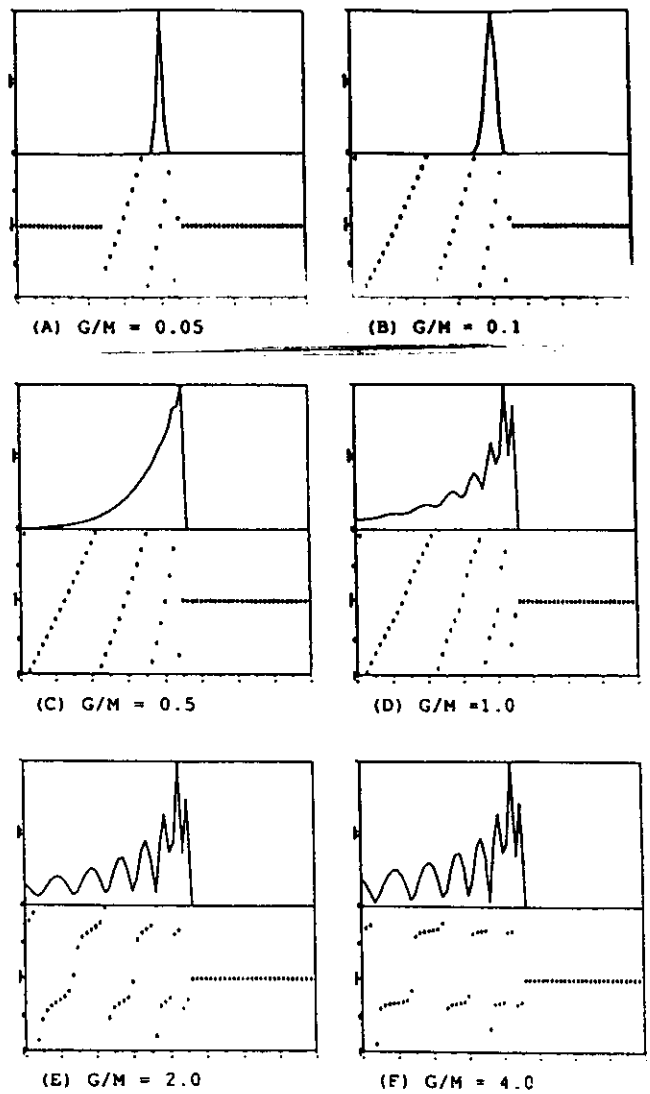

Finally we summarize the diversified methods, which all base on spaced antenna systems and are mostly employed in the interferometer mode. All these set-ups need at least 2 antennas, preferably many more than 2. Multiplex or parallel multi-channel detection is another hardware requirement. These methods are not only applied with VHF MST radars but also with UHF and MF radars.

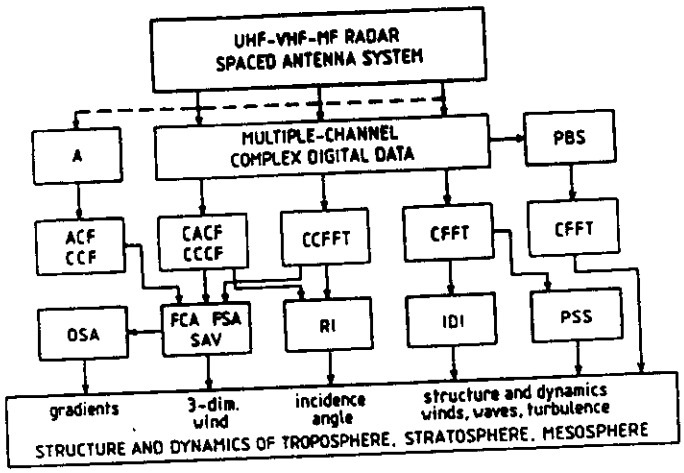

Fig. 1 Methods to analyze radar signals detected with spaced antenna arrays in UHF, VHF and MF radar systems to investigate the structure and dynamics of the lower and middle atmosphere.

The simplest way to deduce wind velocities is just to detect the amplitude A and do the correlation and cross correlation analysis (ACF, CCF). Using quadrature signals (i.e. phase and amplitude) the complex autocorrelation (CACF) and cross correlation (CCCF) analysis is applied and used in the full correlation analysis (FCA) and the full spectrum analysis (FSA) to determine the so-called spaced-antenna velocity (SAV) estimate. The complex cross spectrum (CCFFT) is needed for the FSA. The CCFFT is also used in the radar interferometry (RI) to measure angle of arrival; the mean angle of arrival can also be deduced from the CCCF. The complex cross spectrum is used in the imaging Doppler interferometry (IDI) and in the post-statistics beam steering (PSS), whereas the postset-beam steering (PBS) requires complex transformation before complex spectrum analysis.

All these methods have proved as highly useful and necessary tools for studies of the structure and dynamics of the troposphere, stratosphere and mesosphere.

Simplified sketch how to use NMRF in Interferometer mode

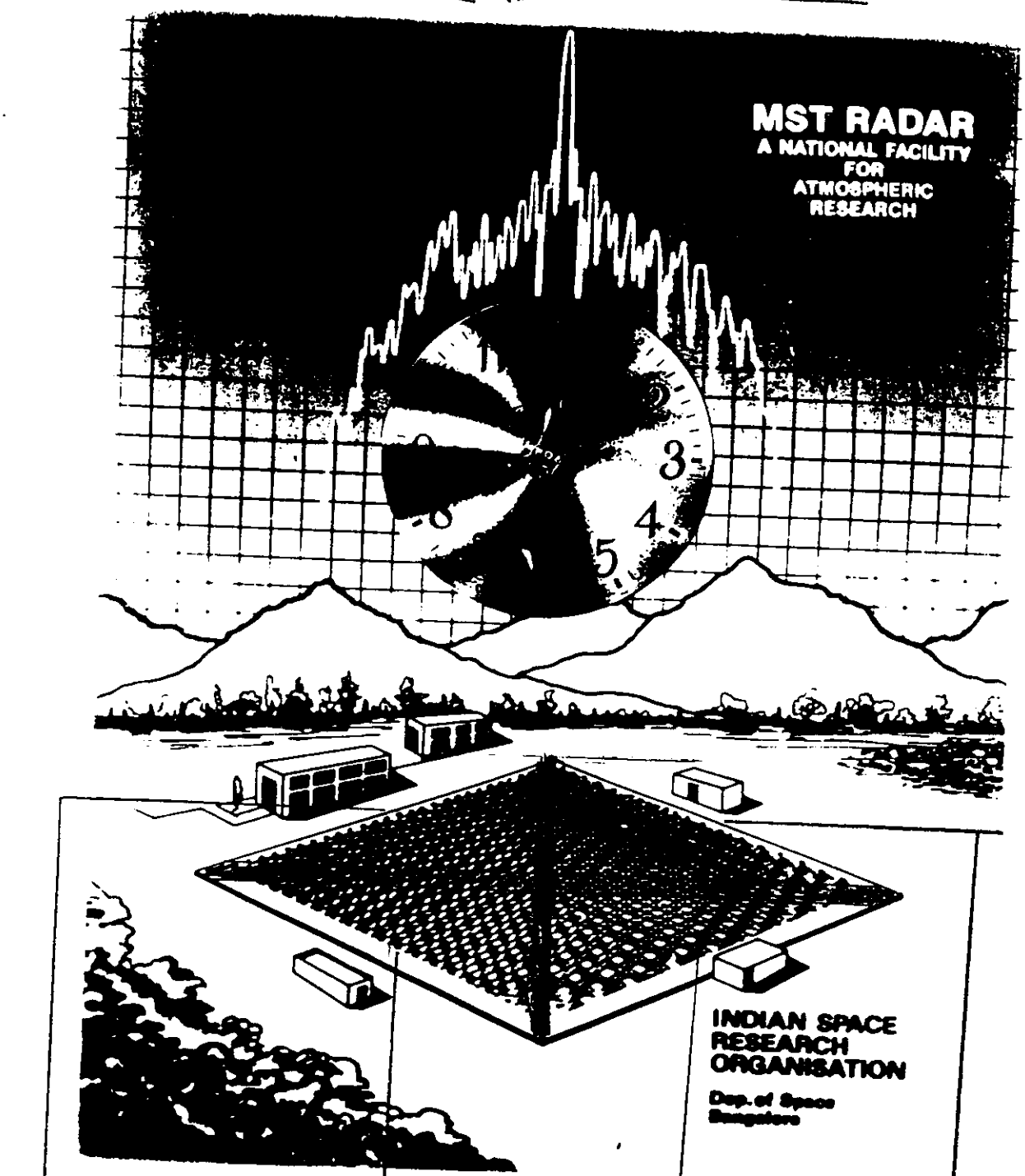

TRX

MPX

TRANSMITTER MODULES

RECEIVER A-D-C (or multiple receivers) → Data Channels ↓

Some Literature on (MST) Radar Interferometry:
(without claiming absolute completeness)

Spatial Domain Interferometry:

Adams, G. W., J. W. Brosnahan, D. C. Walden, and S. T. Nerney, Mesospheric Observations Using a 2.66-MHz Radar as an Imaging Doppler Interferometer: Description and First Results, J. Geophys. Res., **91**, 1671-1683, 1986.

Alcala, C. M., J. Röttger, M. C. Kelley, Spatial interferometry measurements of polar mesosphere summer echoes with the EISCAT VHF radar, Radio Sci., **30**, 1205-1218, 1995.

Briggs, B. H., and R. A. Vincent, Spaced-antenna analysis in the frequency domain, Radio Sci., **27**, 117-129, 1992.

Briggs, B. H., Radar observations of atmospheric winds and turbulence: a comparison of techniques, J. atmos. Terr. Phys., **42**, 823-833, 1980.

Chilson, P. B., R. D. Palmer, M. F. Larsen, C. W. Ulbrich, S. Fukao, M. Yamamoto, T. Tsuda, and S. Kato, First observations of precipitation with a spatial interferometer, Geophys. Res. Lett., **19**, 2409-2412, 1992.

Cohn, S. A., and P. B. Chilson, NCAR Workshop on Multiple-Receiver and Multiple-Frequency Techniques for Wind Profiling, AMS, **76**, 2474-2480, 1995.

Doviak, R. J., R. J. Lataitis, and D. L. Holloway, Cross correlations and cross spectra for spaced antenna wind profilers, Radio Sci., **31**, 157-180, 1996.

Farley, D. T., H. M. Ierkic, and B. G. Fejer, Radar Interferometry: A New Technique for Studying Plasma Turbulence in the Ionosphere, J. Geophys. Res., **86**, 1467-1472, 1981.

Huang, C.M., E. Kudeki, S.J. Franke, C.H. Liu, and J. Röttger, Brightness distribution of midletitude E-region echoe detceted by the Chung-Li VHF radar, J. Geophys. Res., **100**, 14703-14715, 1995.

Hysell, D. L., Radar imaging of equatorial F region irregularities with maximum entropy interferometry, Radio Sci., **31**, 1567-1578, 1996.

Ierkic, H. M., C. Haldoupis, D. R. Moorcroft, and E. Nielsen, Coherent radar interferometry of vertical irregularity structures in the auroral E Region, Radio Sci., **27**, 743-758, 1992.

Kudeki, E., P. K. Rastogi, and F. Sürücü, Systematic Errors in Radar Wind Estimation: Implications for Comparative Measurements, Radio Sci., **28**, 169-179, 1993.

Kudeki, E., F. Sürücü, and R. F. Woodman, Mesospheric wind and aspect sensitivity measurements at Jicamarca using radar interferometry and post-statistic steering techniques, Radio Sci., **25**, 595-612, 1990.

Kudeki, E., Spaced antenna and interferometer methods, isar2 lecture notes, Hilton Head, 1995.

Larsen, M. F., and J. Röttger, VHF Radar Measurements of In-Beam Incidence Angles and Associated Vertical-Beam Radial Velocity Corrections, J. Atmos. Oceanic Technol., **8**, 477-490, 1992.

Larsen, M. F., R. D. Palmer, S. Fukao, R. F. Woodman, M. Yamamoto, T. Tsuda, and S. Kato, An Analysis Technique for Deriving Vector winds and In-Beam Incidence Angles from Radar Interferometer Measurements, J. Atmos. Oceanic Technol., **9**, 1992.

Liu, C. H., J. Röttger, C. J. Pan, and S. J. Franke, A model for spaced antenna observational mode for MST radars, Radio Sci., **25**, 551-563, 1990.

Meek, C. E., and A. H. Manson, Angle-of-arrival oscillations in the meso-sphere as seen by medium frequency (MF) radar, J. atmos. Terr. Phys., **54**, 277-293, 1992.

Meek, C. E., and A. H. Manson, Medium Frequency Interferometry at Saska-toon, Canada, Phys., **35**, 917-921, 1987.

Palmer, R. D., M. F. Larsen, R. F. Woodman, S. Fukao, M. Yamamoto, T. Tsuda, and S. Kato, VHF radar interferometry measurements of vertical velo-city and the effect of tilted refractivity surfaces on standard Doppler measure-ments, Radio Sci., **26**, 417-427, 1991.

Palmer, R. D., M. F. Larsen, E. L. Sheppard, S. Fukao, M. Yamamoto, T. Tsuda, and S. Kato, Poststatistics steering wind estimation in the troposphere and lower stratosphere, Radio Sci., **28**, 261-271, 1993.

Palmer, R. D., R. F. Woodman, S. Fukao, T. Tsuda, and S. Kato, Three-antenna poststatistic steering using the MU radar, Radio Sci., **25**, 1105-1110, 1990.

Pan, C. J., and C. H. Liu, Full spectrum analysis (FSA): Frequency domain analysis for spaced antenna data, 5th Workshop on MST Radar, SCOSTEP, 299-302, 1991.

Pan, C. J., and C. H. Liu, A model for oblique spaced antenna technique for mesosphere-stratosphere-troposphere radars and its applications, Radio Sci., **27**, 131-144, 1992.

Pan, C.J., C.H. Liu, and J. Röttger, Effects of an inhomogeneous wind field on the spaced antenna method, Proc. 7th Workshop on MST radar, SCOSTEP, 396-398, 1996.

Pan, C.J., and J. Röttger, Structures of polar mesosphere summer echoes observed with the EISCAT VHF radar in the interferometer mode, STEP, Proc. 7th Workshop Techn. Scie. Aspects MST radar, 252-255, 1996.

Röttger, J., and R.A. Vincent, VHF radar studies of tropospheric velocities and irregularities using spaced antenna techniques, Geophys. Res. Lett., **5**, 917-920, 1978.

Röttger, J., Investigation of lower and middle atmosphere dynamics with spaced antenna drifts radars, J. atmos. terr. Phys., **43**, 277-292, 1981.

Röttger, J., and H. M. Ierkic, Postset beam steering and interferometer applications of VHF radars to study winds, waves, and turbulence in the lower and middle atmosphere, Radio Sci., **20**, 1461-1480, 1985.

Röttger, J., C.H. Liu, J.K. Chao, A.J. Chen, C.J. Pan, and I-J. Fu, Spatial interferometer measurements with the Chung-Li VHF radar, Radio Sci., **25**, 503-515, 1990.

Röttger, J., C.J. Pan, C.H. Liu, S.Y. Su, and J. Wu, VHF radar interferometer observations of lightning echoes and tropospheric scattering centers, STEP, Proc. 7th Workshop Techn. Scie. Aspects MST radar, 368-371, 1996.

Sheppard, E. L., and M. F. Larsen, Analysis of model simulations of spaced antenna/radar interferometer measurements, Radio Sci., **27**, 759-768, 1992.

Sürücü, F., P.M. Franke, and E. Kudeki, Use of software beam synthesis in multiple-receiver MF radar wind estimation, Radio Sci., **27**, 775-782, 1992.

Van Baelen, J. S., A. D. Richmond, T. Tsuda, S. K. Avery, S. Kato, S. Fukao, and M. Yamamoto, Radar interferometry technique and anisotropy of the echo power distribution: First results, Radio Sci., **26**, 1315-1326, 1991.

Van Baelen, J. S., A. D. Richmond, Radar interferometry technique: Three-dimensional wind measurement theory, Radio Sci., **26**, 1209-1218, 1991.

Valentic, T.A., S.K. Avery, and J.P. Avery, Meteor radar interferometry and array calibration, Proc. 7th MST radar workshop, SCOSTEP, 399-402, 1996.

Woodman, R.F., Inclination of the geomagnetic field measured by incoherent scatter, J. Geophys. Res., **76**, 178-184, 1971.

Frequency Domain Interferometry:

Chilson, P. B., G. Schmidt, Implementation of frequency domain interferometry at the SOUSY VHF radar: First results, Radio Sci., **31**, 263-272, 1996.

Chilson, P. B., A. Muschinski, G. Schmidt, First observations of Kelvin-Helmholtz billows in an upper level jet stream using VHF frequency domain interferometry, Radio Sci., **32**, 1149-1160, 1997.

Chu, Y-H, S. J. Franke, A study of the frequency coherence of stratospheric and tropospheric radar echoes made with Chung-Li VHF radar, Geophys. Res. Lett., **18**, 1849-1852, 1991.

Franke, S. J., J. Röttger, C. LaHoz, C. H. Liu, Frequency domain interferometry of polar mesosphere summer echoes with the EISCAT VHF radar: A case study, Radio Sci., **27**, 417-428, 1992.

Franke, S. J., Pulse compression and frequency domain interferometry with a frequency-hopped MST radar, Radio Sci., **25**, 565-574, 1990.

Kudeki, E., and G. R. Stitt, Frequency domain interferometry: A high resolution radar technique for studies of atmospheric turbulence, Geophys. Res. Lett., **14**, 198-201, 1987.

Palmer, R. D., R. F. Woodman, S. Fukao, M. F. Larsen, M. Yamamoto, T. Tsuda, and S. Kato, Frequency domain interferometry observations of Tropo/Stratospheric scattering layers using the MU Radar: Description and first results, Geophys. Res. Lett., **17**, 2189-2192, 1990.

Palmer, R. D., S. Fukao, M. F. Larsen, M. Yamamoto, T. Tsuda, and S. Kato, Oblique frequency domain interferometry measurements using the middle and upper atmosphere radar, Radio Sci., **27**, 713-720, 1992.
